AD NUMBER
AD338338
CLASSIFICATION CHANGES
TO: unclassified
FROM: confidential
LIMITATION CHANGES
TO: Approved for public release, distribution unlimited
FROM: Distribution authorized to U.S. Gov't. agencies and their contractors; Administrative/Operational Use; 24 JAN 1957. Other requests shall be referred to Atomic Energy Commission, Washington, DC.
AUTHORITY
DNA ltr, 28 Feb 1980; DNA ltr, 28 Feb 1980

AD NUMBER

AD338338

CLASSIFICATION CHANGES

TO

confidential

FROM

secret

AUTHORITY

31 Jan 1969, DoDD 5200.10

UNCLASSIFIED

338338

CLASSIFICATION CHANGED
TO: UNCLASSIFIED-FRD
FROM: CONFIDENTIAL-
AUTHORITY: DNF ltr 28 Feb 80

UNCLASSIFIED

WT-1004 (NOLR-1213)

Docum.
Copy

Operation VIGWAM

: 1.1

CTIONS OF UNDERWATER EXPLOSION PHENOMENA

Issuance Date: January 24, 1957

COMMANDER TASK GROUP 7.3

If this report is no longer needed, return it to
AEC Technical Information Service Extension
P. O. Box 401
Oak Ridge, Tennessee

WT-1004 (NOLR-1918)

This document consists of 74 pages
No. 144 of 205 copies, Series A

Report to the Scientific Director

PREDICTIONS OF UNDERWATER EXPLOSION PHENOMENA

By

H. O. Bray
J. P. Butler
A. N. Gleyzal

Approved by: C. J. AHONSON
Project Officer
Project 1.1

Approved by: A. B. FOCKE
Scientific Director

Approved by: LT COL G. F. WATKINS, USAF
Program I Director

Explosives Research Department
U. S. Naval Ordnance Laboratory
White Oak, Silver Spring, Maryland
May 1956

This document contains restricted data as defined in the Atomic Energy Act of 1954. Its transmittal or the disclosure of its contents in any manner to an unauthorized person is prohibited.

ABSTRACT

This report presents a survey of the various phases of calculations which led to the quantitative prediction of the important underwater explosion parameters for Operation Wigwam.

The Equation of State for Water. The analysis of the explosion phenomena requires a knowledge of the thermodynamic properties of water over an extremely wide pressure range, i.e., from infinity down to the low pressures of an acoustic wave. No equation of state is known which satisfactorily covers this range; therefore five separate pressure ranges were considered.

Region I. At extremely high pressures and temperatures the molecules of water are completely dissociated and ionized. The gas is ideal and monatomic if the small effects of radiation pressure and electrostatic forces are excluded.

Region II. For somewhat lower pressures and temperatures the medium is only partially dissociated and ionized. Laborious equilibrium calculations were made to determine the thermodynamic data in this region. The p-v-T relation necessary for this purpose was obtained from the detonation theory of high explosives, in particular from the explosive hydrazine nitrate which forms H_2O as its principal reaction product.

Region III. At still lower pressures and temperatures the water molecule remains intact. For this range, calculations using the Thomas-Fermi-Dirac theory were made.

Regions IV and V. For pressures from 725,000 psi down to acoustic values, direct experimental measurements notably by Bridgman[8] and Carnevale and Litovitz[10] were used.

Shock Wave Phenomena. These calculations were also separated into several parts. For extremely high pressures the solution of the point blast problem of Taylor[15] is applicable. For lower pressures the three partial differential equations of the spherical fluid motion were integrated. The method was not tractable below a shock pressure of about 450,000 psi (corresponding to a shock radius of 81 ft in Operation Wigwam). The calculations were extended to low pressures by means of the Snay-Matthias[1] shock-wave theory. At very low pressures asymptotic relations, similar to those first derived by Kirkwood and Bethe,[9] were used.

Bubble Phenomena. The energy dissipation (i.e., conversion from mechanical into thermal energy) at the front of the intense shock wave from a point explosion produces the heat which vaporizes the water and forms a steam-filled cavity. This bubble pulsates in a manner similar to that observed for bubbles produced by high explosives. The analysis yielded the maximum bubble radius and the period of the first pulsation as well as the total mass of water evaporated up to the moment of the first bubble maximum. The later bubble phenomena, including the rapid upward migration, can be calculated from data for high-explosive gas bubbles. This establishes an upper limit for the periods and for the migration of a steam bubble. The actual behavior of steam bubbles has been studied with model tests using electric sparks as energy sources. The results of these tests were used to obtain information on the amount of condensation which occurred in Wigwam. It turned out that almost all the vapor must have been condensed before the bubble reached the surface and that the surface phenomena which had some resemblance to the "breakthrough" of a gas bubble were produced by the violent upwelling

of the water which previously surrounded the bubble and which acquired the latter's upward momentum.

In summary, it was found that, in the region where pressures are less than 3000 psi, the calculated pressure-distance curve is similar to one from TNT having about 69 per cent as much energy. In this same region the calculated shock-wave energy flux–distance curve is similar to one from TNT having about 82 per cent as much energy. The maximum bubble radius was calculated to be 376 ft with a first bubble period of 2.88 sec. This period corresponds to that from TNT having 81 per cent as much energy. The amount of water evaporated was calculated to occupy the same volume as a 30-kt TNT sphere.

PREFACE

Project 1.1 of Operation Wigwam was one of four projects (1.1, 1.2, 1.4, and 1.5) for which the Naval Ordnance Laboratory was responsible. Its objective was to determine the principal underwater explosion phenomena to be expected from the explosion, at a depth of 2000 ft in deep water, of an atomic device having a nominal yield of 30 metric kilotons. The successful achievement of this objective enabled at least two extremely important practical results to become available: (1) the determination of proper locations for the targets and instrumentation during the Operation and (2) the development of methods for predicting underwater explosion phenomena from other yields and firing geometries.

This summary report not only gives the predictions which were used in helping to determine the experimental configuration but makes comparisons of these predictions with the actual measurements obtained. The good agreement between theory and experiment indicates that the methods used describe the important phenomena with satisfactory accuracy.

In this report the important equations which have been used in Project 1.1 are summarized and explained. Only simple derivations are given. For a complete analysis the following reports, which describe the subject matter more thoroughly, should be consulted:

NAVORD Report 4181: An Equation of State for Water, by Hans G. Snay and John F. Butler (in preparation).

NAVORD Report 3847: An Equation of State for Water at Extreme Pressures, by J. H. Rosenbaum.

NAVORD Report 4182: A Theory of the Shock Wave Produced by a Point Explosion, by Hans G. Snay (in preparation).

NAVORD Report 4183: An Analysis of Solutions of the Point Blast Problem, by André N. Gleyzal (in preparation).

NAVORD Report 4184: Numerical Analysis of the Underwater Point Blast Problem, by John F. Butler (in preparation).

NAVORD Report 4185: Underwater Explosion Phenomena II: The Parameters of Migrating Gas Bubbles, by Hans G. Snay (in preparation).

The reader who is not interested in mathematical details is invited to read the introductory and summary paragraphs of each chapter of this report, as well as Secs. 3.3 through 3.5. This, together with a study of Table 3.1, the figures, and the glossary (Appendix A), will provide a fair idea of the methods used and the results obtained in this project.

ACKNOWLEDGMENTS

The authors wish to express their gratitude to Joseph Weber (University of Maryland), Frank Matossi [Naval Ordnance Laboratory (NOL)], Sidney G. Reed (Office of Naval Research), and James E. Ablard (NOL) for their generous help and advice in the early phases of this work. Special thanks are due Joseph H. Rosenbaum (NOL) for his investigation of the properties of water using the Thomas-Fermi-Dirac model.

The cooperation of Charles W. Beckett, Harold W. Wooley, Melville S. Green, Joseph Hilsenrath, and Lester Haar [Thermodynamics Section, National Bureau of Standards (NBS)], in the calculation of the high-temperature ideal-gas data is gratefully acknowledged. A highly instructive discussion with John G. Kirkwood helped to clarify the problem of the amount of water evaporated.

M. A. Abramowitz, Joseph H. Wegstein, and John W. Cooper, of the Computational Laboratory, NBS, were responsible for some of the difficult numerical calculations which were made at the NBS for this project.

Mrs. Nancy K. Williams, Bert F. Trafford, Elias V. Schuman, Richard E. McGill, and Irving I. Glick took part in certain phases of the laborious computations which were carried out without benefit of automatic computers. Their work deserves praise and is acknowledged here.

CONTENTS

	Page
ABSTRACT	3
PREFACE	5
ACKNOWLEDGMENTS	7
CHAPTER 1 EQUATION OF STATE FOR WATER	11
1.1 Introduction	11
1.2 Required Data	12
1.3 Region of Extremely High Temperatures and Pressures (Region I)	14
1.4 Equation of State in Region II	14
1.5 Equilibrium Calculations	17
1.6 Calculations Using the Thomas-Fermi-Dirac Model, Region III	19
1.7 Intermediate-pressure Range, Region IV	21
1.8 Range of Very Low Pressures, Region V	23
1.9 Results	26
CHAPTER 2 CALCULATION OF SHOCK-WAVE PHENOMENA	27
2.1 Introduction	27
2.2 Energy Equation and Pressure-Distance Relation	27
2.3 Hydrodynamic Equations	28
2.4 Nature of the Solution	30
2.5 Taylor Case	30
2.6 Expansions Around $\xi = 0$	30
2.7 Polynomials	32
2.8 Determination of ρ	34
2.9 Low-pressure Range	34
2.10 Peak Approximation	38
2.11 Summary and Results	42
CHAPTER 3 BUBBLE PHENOMENA	52
3.1 Introduction	52
3.2 Determination of Maximum Radius	52
3.3 Bubble Parameters and Energy Partition	57
3.4 Bubble Pressure and Temperature, Mass of Water Vaporized	58
3.5 Bubble Migration and Later Bubble Phases	59
3.6 Summary	62

CONTENTS (Continued)

Page

REFERENCES 65

APPENDIX A GLOSSARY OF SYMBOLS 67

ILLUSTRATIONS

CHAPTER 1 EQUATION OF STATE FOR WATER

1.1 Rankine-Hugoniot Relations for Water 20
1.2 Calculations Using the Thomas-Fermi-Dirac Model 22
1.3 Isentropic Exponent 24
1.4 Reduced Internal Energy 25

CHAPTER 2 CALCULATION OF SHOCK-WAVE PHENOMENA

2.1 Reduced Velocity, Pressure, and Density 31
2.2 Determination of β 35
2.3 β for the Entire Pressure Range 40
2.4 Shape Factor, Reduced Total Energy, and Time Factor 41
2.5 Peak Pressure Vs Distance 45
2.6 Time Constant Vs Distance 47
2.7 Distance Vs Time of Arrival 49
2.8 Shock-wave Energy Vs Distance 50

CHAPTER 3 BUBBLE PHENOMENA

3.1 Dissipated Energy, Bubble Energy, and Entropy 55
3.2 Determination of the Maximum Bubble Radius 56
3.3 Migration of the Gas Bubble from 30 Kt of TNT 61

TABLES

CHAPTER 2 CALCULATION OF SHOCK-WAVE PHENOMENA

2.1 Variable Coefficients of Eqs. 2.48, 2.49, and 2.56 39

CHAPTER 3 BUBBLE PHENOMENA

3.1 Shock-front and Shock-wave Parameters 64

CHAPTER 1

EQUATION OF STATE FOR WATER

1.1 INTRODUCTION

An analysis of the explosion phenomena following the firing of an atomic device under water requires the knowledge of the thermodynamic properties of water over a range extending from the extremely high pressures and temperatures occurring immediately after the explosion almost down to the conditions existing in an acoustic wave. No satisfactory equation of state is known which covers the whole range of interest.

In the initial phase, subsequently called Region I, the temperature is so high that the atoms are completely stripped of all their electrons.

At somewhat lower temperatures (Region II), the medium consists of a mixture of the following:

1. Diatomic molecules and radicals formed from hydrogen and oxygen (OH, H_2, O_2, etc.).
2. Monatomic hydrogen and oxygen.
3. Hydrogen and oxygen ions (O^+, O^{+2}, H^-, etc.).
4. Free electrons.
5. Ionized molecules and radicals (O_2^+, OH^-, etc.).

The calculation of the thermodynamic properties of such a mixture requires a knowledge of the concentration of the various constituents of the mixture. The Halford-Kistiakowsky-Wilson (HKW) equation of state is used in this region.

At still lower pressures and temperatures the water molecule remains intact (Region III), but the pressures are still far above the range where direct experimental measurements are possible. In this region the Thomas-Fermi-Dirac (TFD) theory may be used. However, this theory yields acceptable results only at the high-pressure end of this region. Therefore, to obtain data for Region III, interpolations must be made between these calculated high pressures and Region IV, for which measurements by Bridgman are available (up to 725,000 psi). Since the Rankine-Hugoniot curve has little curvature in a ln p – ln v plot, the shock-front data can be readily interpolated graphically.

Region IV has been treated in several publications. Thermodynamic data behind the front are obtained by using a modified form of the isentropic Tait equation and adjusting the constants in this equation in such fashion that the isentropics fit the data at the shock front (Rankine-Hugoniot curve) and at the saturation line.

In the region of relatively low pressures (Region V), where the shock wave behaves almost like an acoustic wave, the thermodynamic properties of water may be inferred from experiments on the velocity of sound in water as a function of pressure.

1.2 REQUIRED DATA

For any shock-wave calculation the Rankine-Hugoniot parameters must be known for the medium in question. The Rankine-Hugoniot conditions are:

the Rankine-Hugoniot adiabatic

$$E_1 - E_0 = \frac{p_1 + 2P_0}{2}(v_0 - v_1), \tag{1.1}$$

the propagation velocity U

$$(U - u_0)^2 = \frac{v_0^2 p_1}{v_0 - v_1}, \tag{1.2}$$

and the particle velocity u_1

$$(u_1 - u_0)^2 = p_1(v_0 - v_1). \tag{1.3}$$

The subscript 1 designates the state directly behind the shock front, and the subscript 0 refers to the state ahead of the front. E is the internal energy per unit mass, p is the excess pressure above the static pressure P_0, and v, the specific volume, is the reciprocal of the density ρ.

The Rankine-Hugoniot adiabatic gives the p-v relation for the thermodynamic change of state at the shock front. To evaluate this, one must know the interrelation between internal energy, pressure, and volume. A formal simplification can be made by introduction of the "reduced internal energy"

$$J = J(p,v) = \frac{E - E_0}{pv}. \tag{1.4}$$

This term will be frequently used in our calculations. It is a dimensionless magnitude related to the heat capacity. For an ideal gas at high temperature the following simple equation holds:

$$J^0 \sim \frac{E}{pv} = \frac{c_v^0}{R} = \frac{1}{\gamma^0 - 1}, \tag{1.5}$$

where the superscript 0 indicates the ideal-gas state, c_v is the heat capacity at constant volume, R is the gas constant, and γ^0 is the ratio of the heat capacities at constant pressure and at constant volume.

The Rankine-Hugoniot adiabatic is generally given by

$$J_1 = \frac{v_0 - v_1}{2v_1}\left(1 + \frac{2P_0}{p_1}\right). \tag{1.6}$$

After rearrangement, we obtain with the use of Eq. 1.5

$$p_1 = P_0 \frac{\frac{\gamma^0 + 1}{\gamma^0 - 1} v_0 - v_1}{\frac{\gamma^0 + 1}{\gamma^0 - 1} v_1 - v_0} - P_0. \tag{1.7}$$

This simple relation holds for ideal gases only. For real gases J must be evaluated from the internal energy,

$$E - E_0 = \int_{T_0}^{T} \sum_i n_i c_{v_i}^0 \, dT + \int_{\infty}^{v} \left[T\left(\frac{\partial p}{\partial T}\right)_v - (p + P_0) \right] dv, \tag{1.8}$$

where n_i is the number of moles of the i*th* constituent in the medium, $c_{v_i}^0$ is its ideal-gas heat capacity, and T is the absolute temperature. The subscript v on the partial differential quotient in the second integral means "at constant volume." A corresponding notation referring, for instance, to constant temperature, entropy, etc., is used in this report. In order to evaluate the first integral, the composition of the medium must be known. This information will be obtained from the equilibrium calculations. The second integral accounts for the imperfect-gas behavior. For its evaluation, we need an equation of state for the imperfect medium. The lower limit of this integral refers to the specific volume at the ideal-gas state.

In considering a nonideal medium, attention must be given to the use of the symbol γ. The customary definition of this symbol is $\gamma = c_p/c_v$. However, in the hydrodynamic literature γ stands for the logarithmic slope of an isentropic. In general, the specific heat ratio is equal to this logarithmic slope only for the case of an ideal gas. In this report the symbol γ will mean the logarithmic slope of an isentropic, i.e.,

$$\gamma = -\left(\frac{\partial \ln p}{\partial \ln v}\right)_S = \frac{c^2}{pv}, \tag{1.9}$$

where c = sound velocity and S = entropy.

The general expression for this isentropic exponent* is

$$\gamma = -\left(\frac{\partial \ln p}{\partial \ln v}\right)_T + \frac{vp}{T}\left(\frac{\partial \ln p}{\partial \ln v}\right)_T^2 \Bigg/ \left(\frac{\partial E}{\partial T}\right)_v. \tag{1.10}$$

The isentropic exponent γ is related to the reduced internal energy J by the following simple equation:

$$\gamma = \frac{1}{J}\frac{p + P_0}{p} + 1 + \left(\frac{\partial \ln J}{\partial \ln v}\right)_S. \tag{1.11}$$

For constant J this equation is equivalent to the ideal-gas relation 1.5. However, in the general case of an imperfect gas, Eq. 1.11 is of little help. It is simpler to calculate γ and J independently using Eqs. 1.10 and 1.8.

The behavior of the Rankine-Hugoniot adiabatic can be expressed in the following concise form:

$$\gamma_{RH} = -\frac{d \ln p_1}{d \ln v_1} = \frac{d \ln p_1}{d \ln \rho_1}. \tag{1.12}$$

This definition is analogous to that of the isentropic exponent γ except that the differential quotient is taken along the Rankine-Hugoniot adiabatic instead of the isentropic. This magnitude will be widely used in the hydrodynamic equations of this report.

The equation for the entropy increment, which is also needed in the hydrodynamic calculations, is

$$\Delta S = S_1 - S_0 = \int_{T_0}^{T_1} \sum_i n_i c_{p_i}^0 \frac{dT}{T} - \int_{p_0}^{p_1 + p_0} \left(\frac{\partial v}{\partial T}\right)_p dp. \tag{1.13}$$

The dissipated enthalpy increment h is defined by

$$h = \frac{p_1}{2}(v_0 + v_1) - \int_0^{p_1} v(p, S = S_1)\, dp. \tag{1.14}$$

---

*The word "exponent" is used loosely here. For constant γ, Eq. 1.9 can be integrated, and it yields the familiar relation $pv^\gamma = \text{const}$. This, however, does not hold for a variable γ.

This magnitude gives the increase of enthalpy after the passage of the shock front when the medium has isentropically returned to the initial pressure P_0. Another expression for h is

$$\begin{aligned} h &= \int_0^{\Delta S_1} T(S,p = 0)\, dS \\ &= \overline{c_p} T_0 (e^{\Delta S_1/\overline{c_p}} - 1), \end{aligned} \tag{1.15}$$

where T_0 is the temperature of the water before the explosion and

$$\overline{c_p} = \frac{\int_{T_0}^{T} c_p\, dT}{T - T_0} \qquad \overline{c_p} = \frac{1}{\ln T/T_0} \int_{T_0}^{T} c_p \frac{dT}{T}. \tag{1.16}$$

For water $\overline{c_p}, \overline{c_p}$ differ only very slightly from the value of the actual heat capacity c_p.

1.3 REGION OF EXTREMELY HIGH TEMPERATURES AND PRESSURES (REGION I)

The equation of the Rankine-Hugoniot adiabatic for an ideal gas, Eq. 1.7, shows that the pressure becomes infinite for a finite value of v_1. Although this relation holds for ideal gases only, it is generally true for shock waves in any medium that v_1 remains finite when pressure and temperature approach infinitely high values. At such conditions, namely, moderate densities but infinitely high temperatures, the medium is completely dissociated and ionized, i.e., the atoms are stripped of all their electrons. The medium consists only of such small particles as electrons, protons, and nuclei. Each of these has but three degrees of freedom; therefore $\gamma = \frac{5}{3}$. The small particle size precludes gas-imperfection effects, and such a plasma would behave like an ideal gas save for the effects of radiation pressure and electrostatic forces. For our purposes it seemed permissible to neglect these effects in this region and to assume that the medium behaves like an ideal monatomic gas. From Eq. 1.7 we obtain

$$\lim_{p_1 \to \infty} v_1 = v_0 \frac{\gamma^0 - 1}{\gamma^0 + 1} = \frac{v_0}{4}.$$

The shock-front data calculated by the methods described in the following paragraphs were extended to infinite pressures by considering the trend of γ_{RH} as a function of v_1. The magnitude

$$\frac{1}{\gamma_{RH}} = -\frac{d \ln v_1}{d \ln p_1}$$

vanishes at $v_1 = v_0/4$ according to the above-discussed behavior of v_1. The simple technique used is described in NAVORD Report 4181.

1.4 EQUATION OF STATE IN REGION II

To evaluate the thermodynamic functions discussed in Sec. 1.2, we need a p-v-T relation from which the necessary differential quotients may be determined. No completely satisfactory equation of state is known for media in Region II, where dissociation and ionization occur. Closest to this range are the thermodynamic states of detonating high explosives whose reaction products attain pressures up to 4.3 million psi, temperatures up to 3000°K, and densities above 2 g cc. Several attempts have been made to describe such thermodynamic conditions by means of an equation of state. All these equations have objectionable features from a theoretical point of view. However, the theory of the detonation process permits a determination of the arbitrary constants in such equations from experimentally measured detonation rates. These rates increase with increasing loading density of the explosive, an effect which is solely due to the imperfect-gas behavior of the reaction products. Therefore this is a sensitive method of determining imperfection terms of high-pressure equations of state.

For this project we have chosen the HKW equation of state because this equation has been tested against detonation data of a great number of explosives with good success.[2] In particular, this equation predicts the detonation rate of the explosive hydrazine nitrate with satisfactory accuracy. The dominant reaction product of this explosive is H_2O. Hence one should expect that this equation is applicable to our problem within the limits of its validity.

The HKW equation of state has the form:

$$(p + P_0)v = \frac{n_g RT}{M_0}(1 + xe^{\beta x})$$

$$x = \frac{k}{M_0 VT} \tag{1.17}$$

$$k = \sum_i n_i k_i \qquad n_g = \sum_i n_i \qquad \alpha = 0.25 \qquad \beta = 0.3,$$

where n_i is the number of moles of the i*th* component in M_0 weight units of gas and k_i is its covolume factor. A few covolume factors have been determined from the measured detonation rates. For our problem it was necessary to estimate the additional covolume factors which could not be determined by this method. A complete account of this is given in NAVORD Report 4181, where a list of the numerical values is found. A few of the more important components are quoted here:

Component	k_i	Component	k_i
H_2O	285	O	100
O_2	300	H	20
H_2	60	O^+	80
O_2^+	255	O^{+2}	65
OH	200	H^+	0

The limits of validity of the HKW equation are given by the imperfection term x. Good results were obtained in the study of detonation phenomena for values of x between 1.7 and 4.2. This range is determined by the experimental data available. It is not unreasonable to assume that acceptable accuracy may be obtained for much lower values of x, since Eq. 1.17 reduces to the perfect-gas law for small x.

If, within these limits of x, the HKW equation is applied to water, higher pressures and temperatures result than those usually obtained for explosion reaction products with the same x. This is due to the low molecular weight of water and the relatively high number of particles in the dissociated state.

The covolume factors noted above hold for the comparatively low temperatures occurring in the detonation of high explosives. One may safely assume that the constituent molecules and atoms are in the ground electronic state under these conditions. This raises the question of whether these covolume factors are applicable to the much higher temperatures occurring in Region II, where appreciable excitation and ionization are encountered.

It is well known that the partition function for an ideal gas diverges at high temperatures. However, it is possible to show,[3,4] that convergent series for the partition function are obtained for imperfect gases. If we consider a HKW gas consisting of only one component and regard the various excited states as separate species, the partition function is given by

$$Q = \frac{P}{1 + xe^{\beta x}} \left[\left(\frac{2\pi m k' T}{h^2}\right)^{3/2} v_0\right] e^{(1-e^{\beta x})/\beta} \sum_i g_i \exp\left(\frac{\epsilon_i}{k'T} - n_g^* \frac{k_i^*}{k^*} xe^{\beta x}\right), \tag{1.18}$$

where k' = Boltzmann constant
h Planck's constant
m = particle mass
g_i statistical weight of the i*th* excited state (i.e., of the i*th* species of the mixture)

ϵ_i = excitation energy of the i*th* excited state
k_i^* = covolume factor for the i*th* excited state
n_i^* = number of moles of atoms which are in the i*th* excited state
$n_g^* = \sum_i n_i^*$ = total number of moles of particles in M_0 grams of the mixture
$k^* = \sum_i n_i^* k_i^*$ = total covolume factor for the mixture.

(The asterisks are used here to emphasize the fact that we are now considering a gas consisting of only one component, for instance O^+, and are regarding the various excited states of this component as separate species). For $x = 0$, Eq. 1.18 reduces to the familiar partition function of an ideal gas. In this case, the sum in Eq. 1.18 is replaced by $\sum_i g_i \exp(\epsilon_i/k'T)$, which is divergent since, although the Boltzmann factors $\exp(\epsilon_i/k'T)$ become smaller with increasing i, the statistical weights g_i become arbitrarily large. For the HKW gas, however, the last factor in the sum in Eq. 1.18 ensures rapid convergence.

To determine how many terms are required in the evaluation of the partition function, Eq. 1.18, we assume that the covolume factor for a given excited state of an atom or ion is proportional to the effective atomic or ionic volume of the atom or ion when in this excited state, when possible (NAVORD Report 4181) to derive the following expression:

$$k^* = \sum_i n_i^* k_i^* = k_0^* n_g^* \frac{\sum_i \frac{V_i}{V_0} g_i \exp\left(\frac{\epsilon_i}{k'T} - n_g^* \frac{V_i}{V_0} \frac{k_0^*}{k^*} x e^{\beta x}\right)}{\sum_i g_i \exp\left(\frac{\epsilon_i}{k'T} - n_g^* \frac{V_i}{V_0} \frac{k_0^*}{k^*} x e^{\beta x}\right)}, \tag{1.19}$$

where V_0 = effective atomic or ionic volume of the component when in its ground state
V_i = effective atomic or ionic volume of the component when in its i*th* excited state
k_0^* = covolume factor for the component when in its ground state.

An evaluation of this equation yielded the interesting result that, for all conditions where the HKW equation of state is applicable, only those excited states which have effective atomic volumes equal to or near that of the ground state contribute significantly to the partition function. Higher terms were found to be entirely negligible, even for a value of x as low as 0.2. The ideal-gas properties for the high temperatures needed in the calculation of the internal energy, the adiabatic exponent, and the entropy were calculated from statistical thermodynamics on this basis. A complete description is given in NAVORD Report 4181, where extensive tables of the pertinent thermodynamic data can also be found.

With the use of the HKW equation of state, the thermodynamic functions of interest to us take the following form:

$$J = \frac{1}{1 + x e^{\beta x}} \left(\frac{1}{T} \int_{T_0}^{T} \frac{\sum_i n_i c_{v_i}^0}{R \sum_i n_i} + \alpha x e^{\beta x} \right). \tag{1.20}$$

$$\gamma = 1 - \left(\frac{\partial \ln n_g}{\partial \ln v}\right)_T + \left(\frac{1 + \beta x}{1 + x e^{\beta x}}\right) x e^{\beta x} \left[1 - \left(\frac{\partial \ln k}{\partial \ln v}\right)_T\right] + \frac{(1 + x e^{\beta x}) \left\{1 + \left(\frac{\partial \ln n_g}{\partial \ln T}\right)_v - \left(\frac{1 + \beta x}{1 + x e^{\beta x}}\right) x e^{\beta x} \left[\alpha - \left(\frac{\partial \ln k}{\partial \ln T}\right)_v\right]\right\}^2}{\frac{\sum_i n_i c_{v_i}^0}{R \sum_i n_i} + \alpha x e^{\beta x} \left\{1 - (1 + \beta x)\left[\alpha - \left(\frac{\partial \ln k}{\partial \ln T}\right)_v\right]\right\}}, \tag{1.21}$$

$$S - S_0 = \int_{T_0}^{T} \sum_i n_i c_{v_i}^0 \frac{dT}{T} - \alpha n_g R \ln \frac{T}{T_0} + n_g R \ln \left(\frac{k}{n_g R} \frac{1}{T_0^{(1+\alpha)}}\right) - n_g R \left(\ln x - \frac{1 - e^{\beta x}}{\beta} - \alpha x e^{\beta x}\right). \tag{1.22}$$

The change of n_g and k with temperature T or with the specific volume v—as well as the concentrations n_i of the various constituents—are determined by equilibrium calculations.

1.5 EQUILIBRIUM CALCULATIONS

The equilibrium constant for an HKW gas is

$$K_j = \prod_i n_i^{\nu_i} = K^0_{p_j}\left(\frac{M_0 v}{RT}\right)^{\sum_i \nu_i} \exp\left[-\left(\sum_i \nu_i\right)\frac{e^{\beta x}-1}{\beta} - \frac{n_g}{k} x e^{\beta x}\sum_i \nu_i k_i + \Phi\right], \quad (1.23)$$

where $\Phi = \dfrac{2.23\times 10^5}{v^{1/2}(DT)^{3/2}}\left(\sum_i \nu_i Z_i^2\right)\left(\sum_i n_i Z_i^2\right)^{1/2}$ = Debye-Hückel correction

or

$$\Phi = \frac{2.589\times 10^6}{T}\left(\frac{\sum_i n_i Z_i}{v}\right)^{1/3}\sum_{i=1}^{Z_j} i^{3/2} \quad \text{= Unsold correction,}$$

where $K^0_{p_j}$ = ideal-gas equilibrium constant for the *j*th reaction
D = dielectric constant
Z_i = valency of the *i*th component
Z_j = valency of the *j*th reaction which must be of the type $x = x^{Z_j} + Z_j e$ (e denotes the free electron).

The ν_i's are the coefficients of the *i*th component in the *j*th reaction equation; those on the right-hand side are counted positive, and those on the left-hand side, negative. The sums containing ν_i run over the terms of the reaction equation. To illustrate this, assume the following reaction:

$$O = O^{+2} + 2e.$$

Here

$$\nu_{O^{+2}} = +1$$
$$\nu_e = +2$$
$$\nu_O = -1$$
$$\sum_i \nu_i = +2$$

and

$$\prod_i n_i^{\nu_i} = \frac{n_{O^{+2}}\, n_e}{n_O},$$

where $n_{O^{+2}}$ is the number of moles of O^{+2} ions, n_e is the number of moles of electrons, and n_O is the number of moles of oxygen atoms in M_0 grams of the mixture. Z_i for O^{+2} is 2, and for e, −1. Hence $\sum_i \nu_i Z_i^2 = 6$. Z_j of this reaction is 2.

The total number of moles of all hydrogen nuclei in one mole of dissociated and ionized water must be equal to 2, and that of all oxygen nuclei must be equal to unity. This can be written as follows:

$$y_1 + \sum_i r_{1i} n_i = 2$$
$$y_2 + \sum_i r_{2i} n_i = 1, \quad (1.24)$$

where r_{1i} is the number of hydrogen nuclei in the ith compound, r_{2i} is the number of oxygen nuclei (e.g., for OH, $r_1 = 1$ and $r_2 = 1$), and where,

$$\begin{aligned} y_1 &= \text{number of moles of hydrogen atoms in } M_0 \text{ grams of the mixture} \\ y_2 &= \text{number of moles of un-ionized oxygen atoms in } M_0 \text{ grams of the mixture} \end{aligned} \tag{1.25}$$

These two magnitudes are reference values. They are by nature the same as certain n_i's for which r_i is unity, and they serve as independent variables. A third reference value of this kind is

$$y_3 = \text{number of moles of electrons in } M_0 \text{ grams of the mixture} = \sum_i n_i Z_i \tag{1.26}$$

Then the concentration of the ith compound is

$$n_i = K_j y_1^{r_{1i}} y_2^{r_{2i}} y_3^{Z_i}. \tag{1.27}$$

There are as many such equations as there are reaction equations. For our calculations, we have considered the following reactions:

j	Reaction	$\sum_i \nu_i$	$\sum_i \nu_i \kappa_i$	$\sum_i \nu_i Z_i^2$	$\sum_{i=1}^{Z_i} I^{j_3}$	r_{1i}	r_{2i}	Z_i
1	$O = O^+ + e$	1	−20	2	1	0	1	1
2	$O = O^{+2} + 2e$	2	−35	6	2.5876	0	1	2
3	$O = O^{+3} + 3e$	3	−46	12	4.6670	0	1	3
4	$O = O^{+4} + 4e$	4	−55	20	7.1872	0	1	4
5	$O = O^{+5} + 5e$	5	−62	30	10.1113	0	1	5
6	$O = O^{+6} + 6e$	6	−100	42	13.4128	0	1	6
7	$O = O^{+7} + 7e$	7	−100	56	17.0724	0	1	7
8	$O = O^{+8} + 8e$	8	−100	72	21.0724	0	1	8
9	$H = H^+ + e$	1	−20	1	2	1	0	1
10	$2O = O_2$	1	100	0	0	0	2	0
11	$2O = O_2^+ + e$	0	55	2	1	0	2	1
12	$2H = H_2$	−1	20	0	0	2	0	0
13	$2H = H_2^+ + e$	0	10	2	1	2	0	1
14	$2H + O = H_2O$	−2	145	0	0	2	1	0
15	$O + H = OH$	−1	80	0	0	1	1	0
16	$O + H + e = OH^-$	−2	110	0	0	1	1	−1
17	$O + H = OH^+ + e$	0	50	2	1	0	1	1
18	$2O + 2H = H_2O_2$	−3		0	0	2	2	0
19	$O + e = O^-$	−1	15	0	0	−1	0	−1
20	$H + e = H^-$	−1	5	0	0	−1	1	−1
21	$2O = O_2^{+2} + 2e$	−1	40	6	2.5876	1	0	2

It will be noted that the reaction equations are arranged in such a way that the first constituent on the right-hand side is that one for which the concentration n_i is given by Eq. 1.27. (For this constituent, i is equal to j.) There are no such equations for O, H, and e, since these are determined by Eqs. 1.24 and 1.26. In all, we have 24 equations for the concentrations of 24 compounds.

Solving these equations numerically is extremely difficult because the equilibrium constant, Eq. 1.23, depends on k and n_g (as defined in Eq. 1.17) which can be enumerated only if the n_i's are known. The problem was coded for a fast electronic computer using an iteration process, but, owing to operational difficulties, only a small part of the computations planned could be

completed. In particular, it was not possible to obtain results for very high temperatures, and the correction for the electrostatic forces, Φ in Eq. 1.23, was not applied.

Nevertheless, it was possible to obtain results in the most important region as illustrated in Fig. 1.1. The machine calculations gave J, $(\sum_i n_i c^0_{v_i})/(R\sum_i n_i)$, n_g, k, and $S - S_0$ directly as functions of p, v, and T. γ was computed by hand from Eq. 1.21 after graphical differentiation of n_g and k. The shock parameters p_1, v_1, and $\gamma_1 = \gamma_1(v_1)$ are readily obtained by graphical interpolation. The results are listed in Table 3.1.

1.6 CALCULATIONS USING THE THOMAS-FERMI-DIRAC MODEL, REGION III

For temperatures lower than those considered in the previous section, the water molecule remains undissociated. The HKW equation of state is still valid under these conditions, but an entirely different approach is possible here, namely, the use of a statistical model for the H_2O molecule.

The statistical model replaces the distinct electron orbitals of an atom by a continuous electron cloud which is treated as a degenerate Fermi gas.

This model is particularly suited for the description of extremely dense matter, and it has been used to obtain information applicable to astrophysical problems. By interpolations between Bridgman's experimental data and the results of theories using this model, it was also possible to obtain information of interest in geophysics.

The same approach was made by J. H. Rosenbaum for water in a calculation made specifically for this project. The following highly idealized structure was assumed for water: Each oxygen molecule is surrounded symmetrically by a certain number of hydrogen molecules, M. Two of these belong to the molecule considered; the rest belong to the nearest neighbors. The medium is thus represented by means of polyhedrons, each having an oxygen nucleus at its center and M hydrogen nuclei on its surface. Each polyhedron is approximated by a sphere, and the hydrogen nuclei are smeared over the surface of this sphere. To be electrically neutral, such a sphere must contain 10 electrons, eight corresponding to the nuclear charge of the oxygen atom and two to that of the two hydrogen atoms. If the radius of this sphere is $\mathcal{R}$, the specific volume is

$$v = \frac{4\pi}{3}\mathcal{R}^3\frac{N_{Av}}{m}, \tag{1.28}$$

where N_{Av} = Avogadro's number and m = molecular weight. The pressure was found from the virial theorem to be:

$$P = \frac{e^2}{4\pi\mu^4}\left\{\frac{Z^2}{10}\left[4\left(\frac{\Psi(x)}{x}\right)^{1/2} - \beta_0\right]\left[\left(\frac{\Psi(x)}{x}\right)^{1/2} + \beta_0\right]^4 - (1-c)\frac{N^2}{x^4}\right\}, \tag{1.29}$$

where e = charge of the electron
μ = Thomas-Fermi unit
x = reduced radius = $\mu\mathcal{R}$
β_0 = exchange correction = $\beta_0(Z)$
Z = charge of the oxygen nucleus at the center = 8
N = charge of the hydrogen nuclei on the surface of the sphere = 2
c = a slowly changing function of M (see Table I in NAVORD Report 3847)

The potential, Ψ, of the electron gas is determined by the TFD equation

$$\Psi'' = x\left[\left(\frac{\Psi}{x}\right)^{1/2} + \beta_0\right]^3 \tag{1.30}$$

with the following boundary conditions

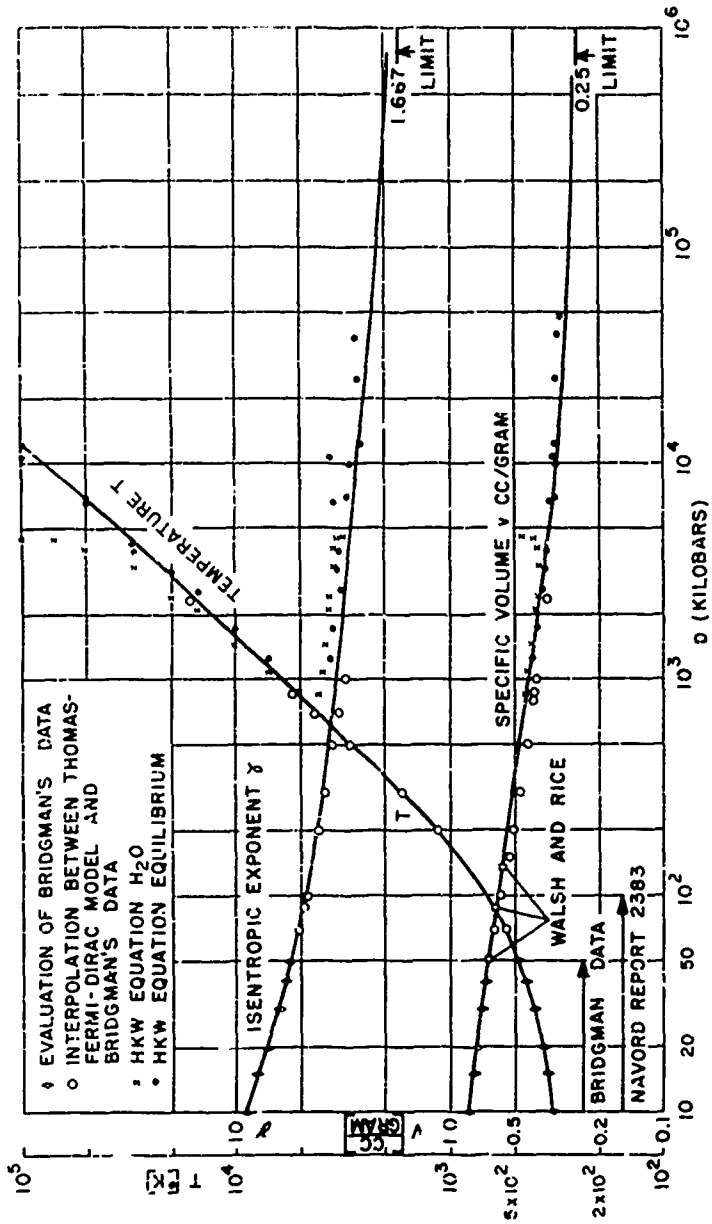

Fig. 1.1—Rankine-Hugoniot relations for water.

$$\Psi(0) = 1$$

$$\psi(x) = x\Psi'(x) - \frac{N}{Z} \qquad \text{at the surface of the sphere} \tag{1.31}$$

The primes indicate differentiation with respect to x. The first boundary condition yields the potential due to the oxygen nucleus at the center; the second condition ensures that N positive charges are distributed over the surface of the sphere and that the whole sphere is electrically neutral, i.e., has Z + N electrons inside the sphere. A more complete discussion is found in NAVORD Report 3847, where an exhaustive list of references is given. The results of these calculations can be summarized as follows:

v, cc/g	P, atm (for M = 8)	P, atm (for M = 12)
0.0988	4.52×10^7	4.55×10^7
0.153	1.78×10^7	1.80×10^7
0.269	5.04×10^6	5.15×10^6
0.700	4.44×10^5	4.73×10^5

It appears that the pressure is relatively insensitive to the choice of M, which depends on the number of nearest neighbors. This is fortunate because the actual structure of water at the high temperatures and, therefore, M are unknown.

The pressures given above refer to absolute zero temperature. For higher temperatures the "thermal" pressure p_T must be added. In NAVORD Report 3847 the following expression is derived:

$$p_T = -\frac{kT}{v}\left[\frac{v}{4}\left(\frac{\partial v}{\partial p}\right)_{T\approx 0}\left(\frac{\partial^2 p}{\partial v^2}\right)_{T\approx 0} + \frac{1}{3}\right] \tag{1.32}$$

This can be evaluated easily for the degenerate electron gas and leads to the simple formula

$$p_T = 27.35\,\frac{T}{v} \tag{1.33}$$

This equation of state (namely, Eqs. 1.28, 1.29, and 1.33 combined) is valid only for extremely high pressures. Data for Region III can be obtained by interpolations between these extremely high pressures and Region IV, for which experimental data exist. Figure 1.2 shows such an interpolation. It is now possible to derive the shock-front parameters as well as the other data by the methods described in the previous paragraphs. These data apply only for those temperatures where no substantial dissociation of the water molecule takes place. The final results are shown in Fig. 1.1; p_1 and γ_1 as obtained from the TFD model are lower by a small amount than those obtained from the calculations with the HKW equation. But, in general, the agreement is as good as can be expected, considering the approximate nature of both approaches. Of particular interest is the agreement in the temperature; because, according to a theory of Jones,[5] even a crude evaluation of detonation rates is expected to give results of fair accuracy for the p-v data, whereas good results for the temperature can be obtained only if the form of the equation of state is correct. Our results may, with a certain reservation, indicate that the form of the HKW equation is approximately correct.

1.7 INTERMEDIATE-PRESSURE RANGE, REGION IV

The equation of state at pressures of about 100 kb and below has been treated in various publications (see, for instance, references 6 to 8). We have used the isentropic Tait equation as proposed by Kirkwood and Bethe, Eq. 2.2 of reference 9, to map out γ and J in the region

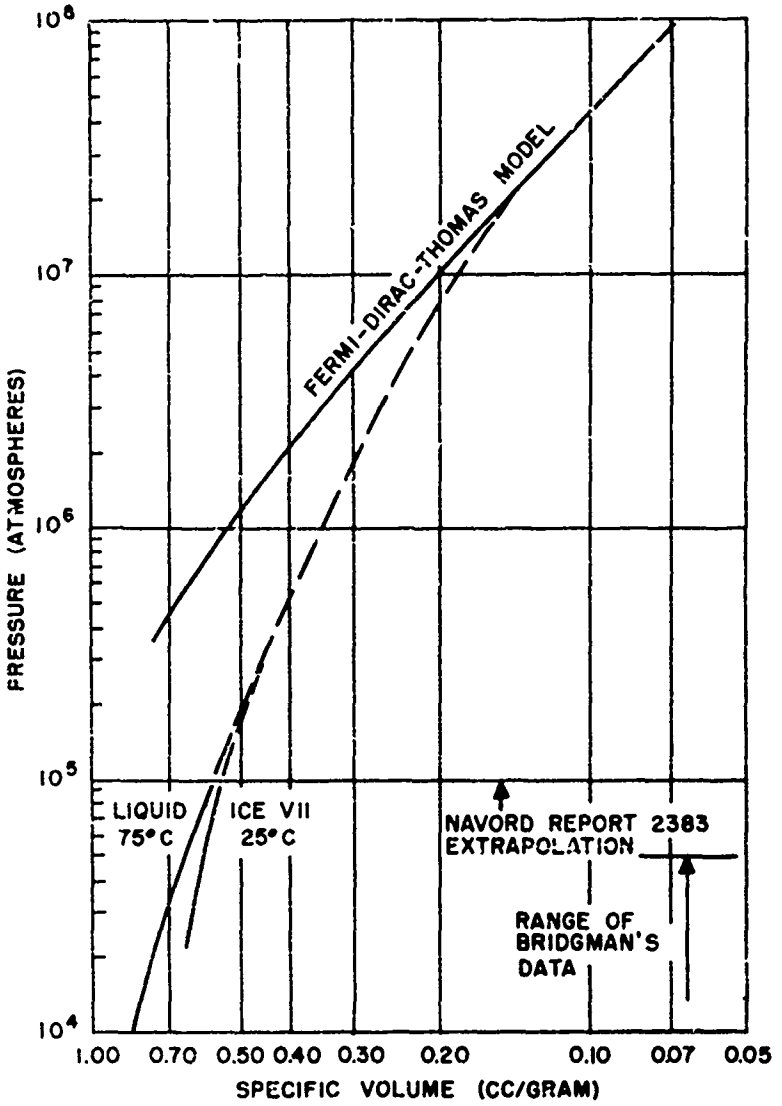

Fig. 1.2—Calculations using the TFD model.

between the shock front and the saturation line. It was necessary to use variable coefficients and exponents in this equation. This Tait equation failed completely in and near the region where the HKW equation was used. The results are shown in Figs. 1.3 and 1.4.

1.8 RANGE OF VERY LOW PRESSURES, REGION V

For the sake of completeness, the relations which hold for low pressures, where the shock wave behaves almost like an acoustic wave, are given below. If the sound velocity c changes linearly with pressure, i.e.,

$$c = c_0(1 + \zeta p), \tag{1.34}$$

the following relations can be derived:

$$\frac{v_0 - v}{v} = \frac{p}{\rho_0 c_0^2} \frac{1}{1 + \zeta p} \tag{1.35}$$

$$\gamma \frac{v_0 - v}{v_0} = 1 + \zeta p \tag{1.36}$$

$$\gamma \frac{v_0 - v}{v} = 1 + \left(\zeta + \frac{1}{\rho_0 c_0^2}\right) p. \tag{1.37}$$

For very low pressures the following first-order approximations can be derived for the shock front:

$$\lim_{\rho_1 \to \rho_0} \gamma_{RH}\left(\frac{\rho_1 - \rho_0}{\rho_1}\right) = \lim_{\rho_1 \to \rho_0} \gamma_1\left(\frac{\rho_1 - \rho_0}{\rho_1}\right) = 1 + a_1\left(\frac{\rho_1 - \rho_0}{\rho_0}\right) \tag{1.38}$$

$$\lim_{\rho_1 \to \rho_0} \gamma_1\left(\frac{\rho_1 - \rho_0}{\rho_0}\right) = 1 + a_2\left(\frac{\rho_1 - \rho_0}{\rho_0}\right), \tag{1.39}$$

where

$$\begin{aligned} a_1 &= \zeta \rho_0 c_0^2 \\ a_2 &= 1 + a_1. \end{aligned} \tag{1.40}$$

Using these first-order approximations, we obtain for the dissipated enthalpy increment h (see definition in Eq. 1.14)

$$\lim_{\rho_1 \to \rho_0} \rho_0 h = \frac{a_2}{6} p_1 \left(\frac{\rho_1 - \rho_0}{\rho_0}\right)^2. \tag{1.41}$$

In these equations we have used the relation $v_1 = 1/\rho_1$.

Strictly speaking, the magnitude ζ as defined by Eq. 1.34 refers to the change of sound velocity along an isentropic. For low pressures, however, it is permissible to use values of ζ which are obtained by measuring sound velocities as functions of pressure at constant temperature. Experiments recently completed at the Naval Ordnance Laboratory[10] give

$$\zeta = 0.106 \text{ kb}^{-1}.$$

This value holds for sea water as well as for fresh water over a wide temperature range (0 to 40°C) which includes the range in which we are interested. For a_1 we have used

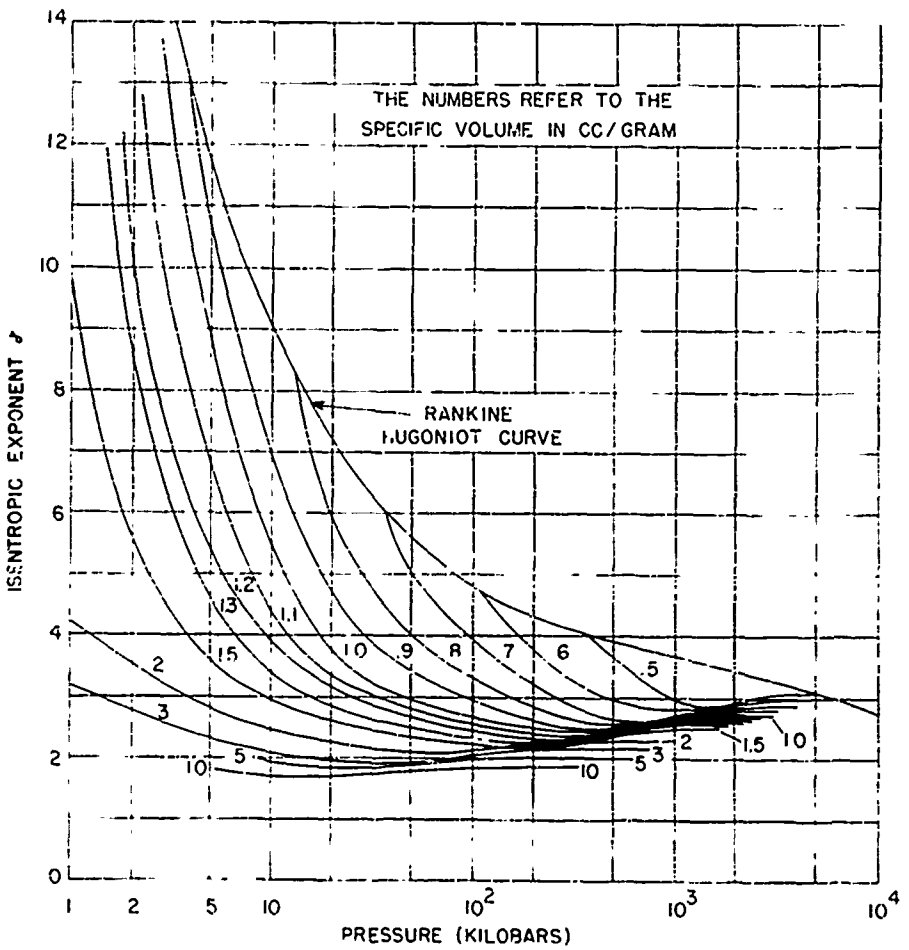

Fig. 1.3—Isentropic exponent.

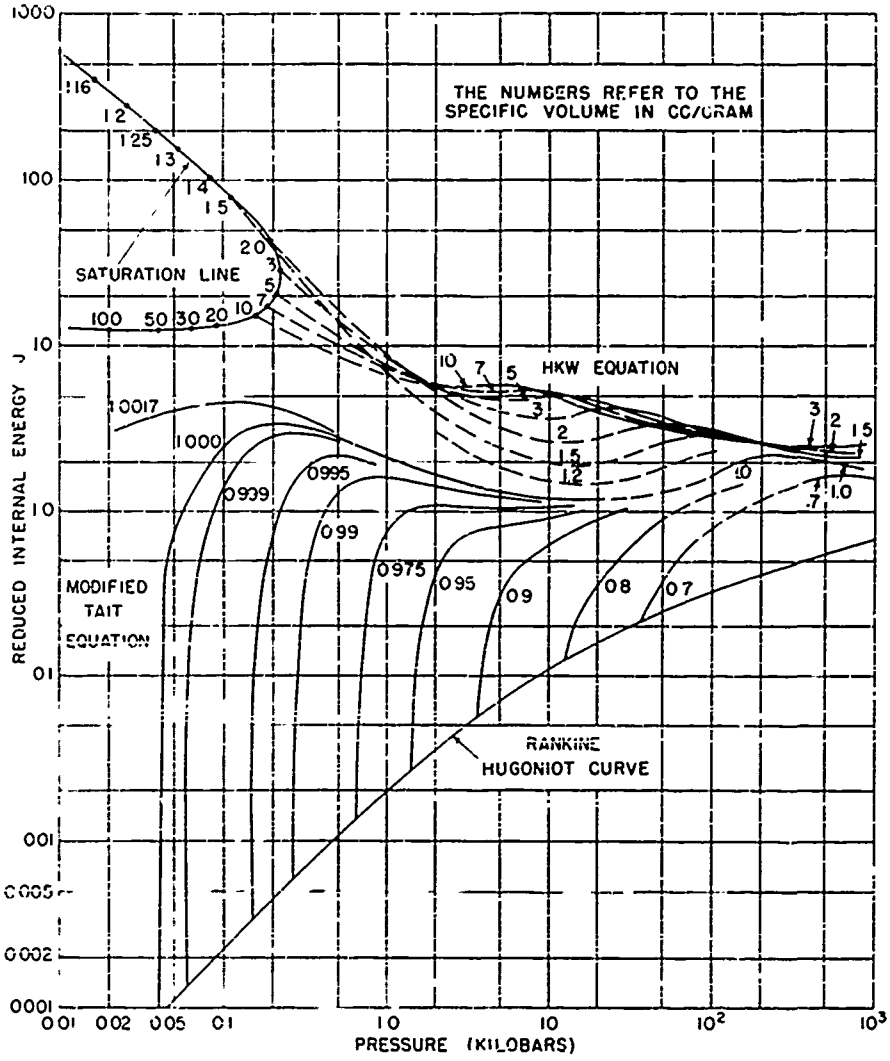

Fig. 1.4—Reduced internal energy.

$a_1 = 2.376$.

This value holds for fresh water at 20°C and also for sea water at about 8°C. The latter case corresponds to the conditions at Wigwam, whereas the former case is that for which the thermodynamic calculations were made. It seems reasonable to assume that, for high pressures where the pertinent information is lacking, our calculations which were made for fresh water at 20°C hold adequately for sea water at a temperature of 8°C. Since in the shock-wave calculations only the ratio ρ_1/ρ_0 occurs and the absolute value of the density of the ambient medium does not appear, these calculations are relatively insensitive to the ambient temperature.

1.9 RESULTS

The final results for the shock-front parameters are listed in Table 3.1 and are shown in Fig. 1.1. The isentropic exponent γ and the reduced internal energy J for the whole region of our interest are presented in graphical form in Figs. 1.3 and 1.4.

In general, thermodynamic functions obtained from equilibrium calculations are not smooth. With increasing temperature, different dissociation and ionization levels are reached, and therefore the number of particles changes discontinuously; this results in irregularities in the graphical representation of such functions. For practical reasons we have used smoothed data in the hydrodynamic calculations, and Table 3.1 gives such data with these irregularities eliminated. In the region where there is an overlap in the data given by the TFD model and the HKW equation, we have given the latter full preference (except for the isentropic exponent γ), although the differences are not very large. The HKW p-v data are in excellent agreement with the experimental results of Walsh and Rice,[11] who measured propagation and particle velocities of strong shock waves in water. Their results are indicated in Fig. 1.1.

The results of our equilibrium calculations of the isentropic exponent γ show a greater scatter than that obtained for the other thermodynamic variables. This scatter in γ may be attributed to variations caused by the inclusion of excited states and to uncertainties introduced by the graphical differentiations required (see Eq. 1.21). For γ to vary smoothly from the low-pressure region to the value 1.666 at infinite pressure, it was necessary to use an average between the data obtained from the TFD model and the HKW values (see Fig. 1.1).

γ varies from the value 1.666 (at infinite pressure) to infinity (in the limit of zero excess pressure). Attempts were made to introduce new variables so that a more well-behaved function could be used in place of γ. It was not possible to obtain substantially simplified relations, and thus it was necessary to use the calculated values of γ in tabular or graphical form.

CHAPTER 2

CALCULATION OF SHOCK-WAVE PHENOMENA

2.1 INTRODUCTION

The calculations of the shock-wave phenomena produced by an atomic burst were based on the idealizing concept of a point explosion, i.e., an infinitely small explosive charge delivers a finite amount of energy instantaneously. At the first moment, such a concentrated energy discharge produces infinitely high pressures and temperatures. An instant later, these become finite and subsequently run through the range which would occur in an atomic explosion. It is this later range which we shall try to calculate here, since initially the model of a point explosion is unrealistic even for atomic explosions, which produce high but finite temperatures and do not release their energy at a single point.

An important consideration for atomic explosions is the question of the energy transport by radiation. A study of this question by Weber[12] showed that, for underwater explosions, radiation phenomena are much less important than for air bursts. In our calculations we have neglected radiation entirely and have assumed that the energy of the burst is transmitted from one particle to the next by pressure forces only. This is a satisfactory assumption once the shock front has traveled a certain distance, although it is a poor assumption for the early stage of the explosion and for the region near the center for later stages. Since we are not concerned with these phenomena here and since they do not affect the results of interest to us, the neglect of radiation seems appropriate.

The calculations described in this chapter deal with the task of integrating the spherical blast-wave equations with variable isentropic exponent γ. They had to be carried out without the benefit of an electronic computer, and so certain approximations were necessary. However, none of the approximations made seem to be of a serious nature. The greatest advantages in tractability were achieved by the introduction of reduced variables and a corresponding transformation of the hydrodynamic equations.

2.2 ENERGY EQUATION AND PRESSURE-DISTANCE RELATION

The total energy contained within the sphere bounded by the shock front is constant and is equal to Q, the hydrodynamic yield of the weapon. All particles within this sphere have kinetic as well as internal energy. The law of conservation of energy may be written:

$$Q = 4\pi \int_0^{r_1} \left[\frac{\rho u^2}{2} + \rho(E - E_0)\right] r^2\, dr = \text{constant}, \tag{2.1}$$

where E denotes the internal energy per unit mass for particles inside the sphere of radius r_1 and E_0 denotes the internal energy per unit mass of the ambient water. We transform this equation by introduction of the following reduced variables:

$$\psi = \text{reduced pressure} = \frac{\text{pressure}}{\text{shock-wave peak pressure}} = \frac{p}{p_1}$$

$$\varphi = \text{reduced particle velocity} = \frac{\text{velocity}}{\text{peak velocity}} = \frac{u}{u_1}$$

$$\chi = \text{reduced density} = \frac{\text{density}}{\text{peak density}} = \frac{\rho}{\rho_1}$$

$$\xi = \text{reduced distance} = \frac{\text{radial distance}}{\text{radial distance of shock front}} = \frac{r}{r_1}$$

$$J = \text{reduced internal energy} = \frac{E - E_0}{p}\rho \qquad \text{(see Eq. 1.4).}$$

With these new variables and with the use of the Rankine-Hugoniot conditions given in Eqs. 1.1 and 1.3, Eq. 2.1 takes the form

$$Q = \frac{4\pi}{3} r_1^3 p_1 \frac{\rho_1 - \rho_0}{2\rho_0} \eta_1, \tag{2.2}$$

where η_1 is the reduced total energy defined by

$$\eta_1 = 3\int_0^1 \left(\varphi^2\chi + \frac{2J\rho_0}{\rho_1 - \rho_0}\psi\right)\xi^2\, d\xi. \tag{2.3}$$

Since p_1 is a function of ρ_1, Eq. 2.2 provides a convenient relation for the peak pressure p_1 as a function of distance r_1 for any given yield Q, once η_1 is known.

2.3 HYDRODYNAMIC EQUATIONS

To determine η_1 we have to find solutions of the partial differential equations of the spherical fluid motion

$$u_t + uu_r + \frac{1}{\rho}p_r = 0 \tag{2.4}$$

$$\rho_t + u\rho_r + \rho u_r + \frac{2\rho u}{r} = 0 \tag{2.5}$$

$$p_t + up_r = \gamma(p,\rho)(\rho_t + u\rho_r) \tag{2.6}$$

and their boundary conditions, which are the Rankine-Hugoniot conditions, Eqs. 1.1 to 1.3. In the above equations, p denotes the excess pressure above the hydrostatic pressure P_0. γ is the isentropic exponent discussed in Sec. 1.2.

By introduction of the reduced variables φ, χ, and ψ and the Rankine-Hugoniot conditions, the hydrodynamic equations, Eqs. 2.4 to 2.6, can be brought into the following form:

$$\frac{\partial\varphi}{\partial\xi} = \frac{\varphi}{\xi}\,\frac{\frac{\partial\psi}{\partial\xi}\frac{1}{\varphi\chi}\frac{\rho_0}{\rho_1 - \rho_0} + L_1 + G_1\frac{\partial \ln\varphi}{\partial \ln\rho_1}}{\frac{\rho_1}{\rho_1 - \rho_0} - \frac{\varphi}{\xi}} \tag{2.7}$$

$$\frac{\partial \chi}{\partial \xi} = \frac{\chi}{\xi} \frac{\frac{\partial \varphi}{\partial \xi} + \frac{2\varphi}{\xi} + G_1 + G_1 \frac{\partial \ln \chi}{\partial \ln \rho_1}}{\frac{\rho_1}{\rho_1 - \rho_0} - \frac{\varphi}{\xi}}, \tag{2.8}$$

$$\frac{\partial \psi}{\partial \xi} = \frac{\psi}{\xi} \frac{\gamma\left(\frac{\partial \varphi}{\partial \xi} + \frac{2\varphi}{\xi}\right) + H_1 + G_1 \frac{\partial \ln \psi}{\partial \ln \rho_1}}{\frac{\rho_1}{\rho_1 - \rho_0} - \frac{\varphi}{\xi}}, \tag{2.9}$$

where

$$H_1 = H_1(\rho_1, \beta) = \frac{r_1}{u_1} \frac{d \ln p_1}{dt} = \frac{-3\left(\frac{\rho_1}{\rho_1 - \rho_0}\right)}{1 + \frac{1}{\gamma_{RH}} \frac{\rho_1}{\rho_1 - \rho_0} (1 + \beta)} \tag{2.10}$$

$$G_1 = G_1(\rho_1, \beta) = \frac{r_1}{u_1} \frac{d \ln \rho_1}{dt} = \frac{1}{\gamma_{RH}} H_1 \tag{2.11}$$

$$L_1 = L_1(\rho_1, \beta) = \frac{r_1}{u_1} \frac{d \ln u_1}{dt} = \frac{H_1}{2}\left(1 + \frac{1}{\gamma_{RH}} \frac{\rho_0}{\rho_1 - \rho_0}\right) \tag{2.12}$$

$$\gamma = \gamma(\rho_1, \chi, \psi) \qquad \gamma_{RH} = \gamma_{RH}(\rho_1) \tag{2.13}$$

$$\beta = \frac{\rho_1 - \rho_0}{\rho_1} \frac{d \ln \eta_1}{d \ln \rho_1}. \tag{2.14}$$

It will be noted that the time variable has been eliminated from these equations and may be regarded as replaced by the peak density ρ_1. The boundary conditions are simply

$$\left.\begin{aligned} \varphi &= 1 \\ \chi &= 1 \\ \psi &= 1 \end{aligned}\right\} \xi = 1 \qquad \left.\begin{aligned} \varphi &= 0 \\ \frac{\partial \psi}{\partial \xi} &= 0 \end{aligned}\right\} \xi = 0. \tag{2.15}$$

(The latter two boundary conditions are obtained from symmetry considerations at the center of the sphere and from the hydrodynamic Eq. 2.4.) It follows that the derivatives of φ, χ, and ψ with respect to ρ_1 vanish for $\xi = 1$. Thus, for $\xi = 1$, Eqs. 2.7 to 2.9 become

$$\varphi_1' = \left(\frac{\partial \varphi}{\partial \xi}\right)_{\xi=1} = \frac{2\gamma_1 + H_1 + L_1}{\frac{\rho_0}{\rho_1 - \rho_0} - \gamma_1} \tag{2.16}$$

$$\chi_1' = \left(\frac{\partial \chi}{\partial \xi}\right)_{\xi=1} = \frac{\rho_1 - \rho_0}{\rho_0}(\varphi_1' + 2 + G_1) \tag{2.17}$$

$$\psi_1' = \left(\frac{\partial \psi}{\partial \xi}\right)_{\xi=1} = \frac{\rho_1 - \rho_0}{\rho_0}[\gamma_1(\varphi_1' + 2) + H_1]. \tag{2.18}$$

These differential quotients are functions of ρ_1 and β, where β is an as yet undetermined function of ρ_1, as indicated by Eq. 2.14.

2.4 NATURE OF THE SOLUTION

In order to see how β is related to the solution of our problem, we use the following consideration: If $\gamma(p,\rho)$ is an analytic function at the shock front, we can calculate the higher derivatives φ_1', φ_1'', ..., χ_1', χ_1'', ..., ψ_1', ψ_1'', ... All are functions of ρ_1 and β. Assuming φ, χ, and ψ to be analytic, we can make a Taylor expansion around $\xi = 1$:

$$\varphi(\xi,\rho_1,\beta) = 1 - \varphi_1'(1-\xi) + \frac{\varphi_1''}{2}(1-\xi)^2 - \frac{\varphi_1'''}{6}(1-\xi)^3 + \ldots \tag{2.19}$$

$$\chi(\xi,\rho_1,\beta) = 1 - \chi_1'(1-\xi) + \frac{\chi_1''}{2}(1-\xi)^2 - \frac{\chi_1'''}{6}(1-\xi)^3 + \ldots \tag{2.20}$$

$$\psi(\xi,\rho_1,\beta) = 1 - \psi_1'(1-\xi) + \frac{\psi_1''}{2}(1-\xi)^2 - \frac{\psi_1'''}{6}(1-\xi)^3 + \ldots \tag{2.21}$$

Introduction of these expansions into the integral, Eq. 2.3, for the reduced total energy η_1 yields η_1 as a function of ρ_1 and β. This, by virtue of Eq. 2.14, is an ordinary differential equation of the first order for η_1. Therefore this approach has reduced the three partial differential equations to one ordinary differential equation.

For practical calculations this method is not suitable because the coefficients of the high-order terms in the expansions, Eqs. 2.19 to 2.21, are too complicated. Therefore a combination of expansions around $\xi = 0$ and $\xi = 1$ was used in this project, as will be described in the following sections. The differential equation for η_1 was solved graphically by the method of isoclines.

2.5 TAYLOR CASE

In Sec. 1.3 we have seen that, for infinitely high pressures, the density ρ_1 directly behind the shock front approaches a finite value, $\rho_1 = 4\rho_0$. We also have $\gamma = 5/3$ and $1/\gamma_{RH} = 0$. In this case the three partial differential equations, Eqs. 2.7 to 2.9, become ordinary differential equations. This is the well known Taylor[13] solution for strong point blast waves.

We shall assume that the Taylor solution gives the density, velocity, and pressure distribution within the infinitesimal sphere at $t = 0$. This is an idealizing approximation because actual explosions, even from concentrated energy sources, cannot have such distributions from the beginning. However, it seems safe to assume that the actual distributions converge quickly to those which are calculated with the assumption of an initial Taylor solution.

Since infinitely high temperatures are assumed to prevail throughout the sphere of disturbance at $t = 0$, the isentropic exponent γ is constant within this sphere and equals $5/3$. For constant γ the differential equations can be solved in closed form (see NAVORD Report 4182). The solution is shown in Fig. 2.1 in the curves labeled $\rho_1 = 4\rho_0$. It is interesting that the density vanishes at the center of the explosion. The same holds true at later times when the shock front has traveled to larger distances.

2.6 EXPANSIONS AROUND $\xi = 0$

The Taylor solution can be given not only in closed form (which is discussed in NAVORD Report 4182) but also in the form of infinite series:

$$\begin{aligned} \varphi &= C_0\xi + C_1\xi^{m+3} + C_2\xi^{2m+5} + \ldots \\ \chi &= B_0\xi^m + B_1\xi^{2m+2} + B_2\xi^{3m+4} + \ldots \\ \psi &= A_0 + A_1\xi^{m+2} + A_2\xi^{2m+4} + \ldots, \end{aligned} \tag{2.22}$$

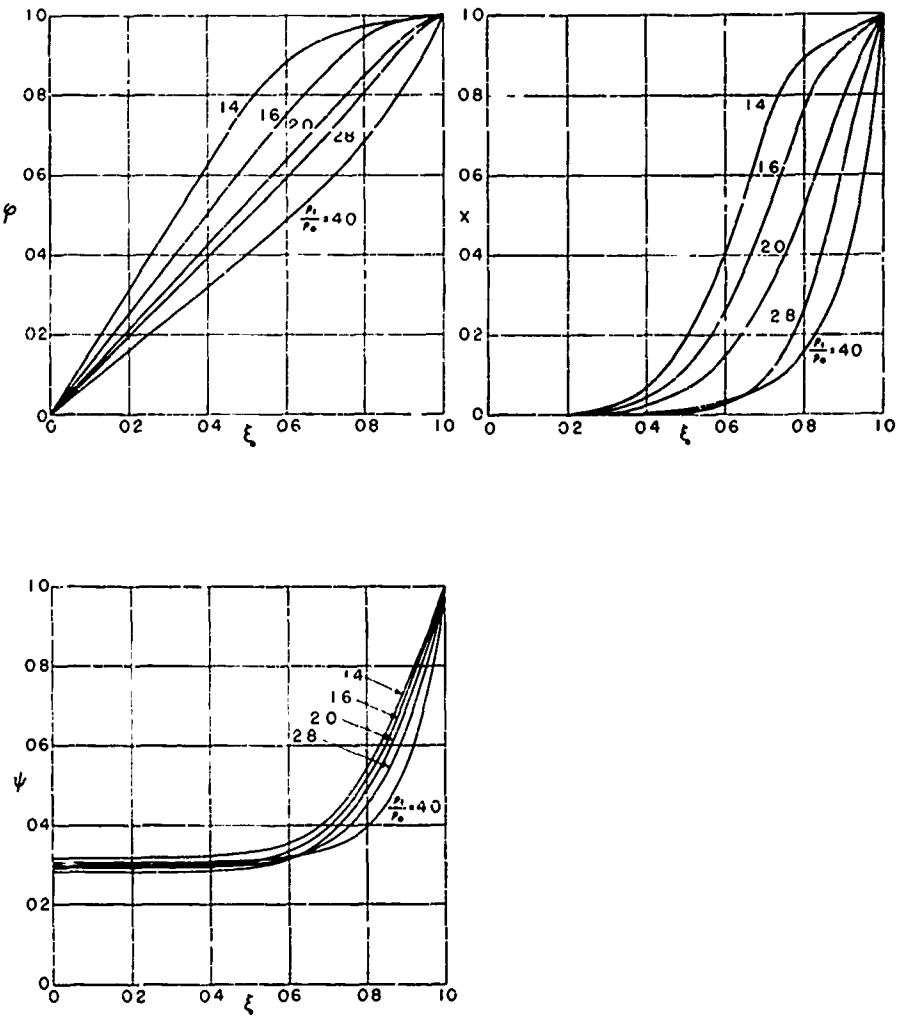

Fig. 2.1 — Reduced velocity, pressure, and density.

where

$$m - \frac{3}{\gamma^0 - 1} = 4.5$$

Explicit expressions for the first few coefficients are also given in NAVORD Report 4182. The numerical values are $A_0 = 0.306$, $A_1 = 0.320$, $B_0 = 0.343$, $C_0 = 0.800$, and $C_1 = 0.229$.

In NAVORD Report 4183 it is shown that such expansions may be used to express the desired solutions of the partial differential equations, Eqs. 2.7 to 2.14. For this general case, that is, $1/\gamma_{RH} \neq 0$, the coefficients in Eq. 2.22 are functions of ρ_1. Substituting these expansions into the partial differential equations and equating like powers of ξ yields a set of ordinary differential equations in the coefficients A_i, B_i, and C_i. The first three of these are

$$3\gamma_0 C_0 + H_1 + G_1 \frac{d \ln A_0}{d \ln \rho_1} = 0 \tag{2.23}$$

$$m\left(\frac{\rho_1}{\rho_1 - \rho_0} - C_0\right) - 3C_0 - G_1 - G_1 \frac{d \ln B_0}{d \ln \rho_1} = 0 \tag{2.24}$$

$$\frac{\rho_0}{\rho_1 - \rho_0} \frac{m+2}{B_0 C_0} A_1 + L_1 - \frac{\rho_1}{\rho_1 - \rho_0} + C_0 + G_1 \frac{d \ln C_0}{d \ln \rho_1} = 0. \tag{2.25}$$

These are three equations in the four unknowns A_0, A_1, B_0, and C_0. For each additional differential equation added to this system, one more unknown is introduced. Therefore the expansion around $\xi = 0$ is undetermined unless additional information is incorporated.

As described in NAVORD Report 4184, this may be accomplished in several different ways. The most successful method tried uses Eq. 2.7. After solving for $\partial\psi/\partial\xi$ and integrating from $\xi = 0$ to $\xi = 1$, we obtain

$$A_0 = 1 - \frac{\rho_1}{\rho_0} \int_0^1 \chi\xi \frac{\partial\varphi}{\partial\xi} d\xi + \frac{\rho_1 - \rho_0}{\rho_0} \int_0^1 \left(\frac{\partial\varphi}{\partial\xi} + L_1 + G_1 \frac{\partial \ln \varphi}{\partial \ln \rho_1}\right) \varphi\chi \, d\xi. \tag{2.26}$$

2.7 POLYNOMIALS

Since the solutions can be expressed by means of expansions around $\xi = 1$ (Eqs. 2.19 to 2.21) and around $\xi = 0$ (Eq. 2.22), one may construct approximate solutions by using relatively few terms of each and merging these together in the intermediate range. One of the simplest ways to do this is to use the expansion around $\xi = 0$ for the entire range of ξ, but to determine a certain number of the coefficients in such a way that the boundary conditions, Eq. 2.15, are fulfilled as well as the behavior near $\xi = 1$, as given by the first-order derivatives, Eqs. 2.16 to 2.18, and any higher order derivatives which one may wish to include.

If only first-order terms are used, we employ a four-term polynomial for χ and a three-term polynomial for φ and J:

$$\begin{aligned} \varphi &= C_0\xi + C_1\xi^{m+3} + C_2\xi^{2m+5}, \\ \chi &= B_0\xi^m + B_1\xi^{2m+2} + B_2\xi^{3m+4} + B_3\xi^{4m+6}, \\ J &= A_0 + A_1\xi^{m+2} + A_2\xi^{2m+4}. \end{aligned} \tag{2.27}$$

There are then 10 coefficients to be determined, for which we have the following conditions:

1. Three boundary conditions, Eq. 2.15.
2. Three first-order derivatives at $\xi = 1$, Eqs. 2.16 to 2.18.
3. Two first-order differential equations, Eqs. 2.23 and 2.24.

One further condition can be obtained from the fact that the mass of the sphere which is bound by the shock front is equal to that of an equally large sphere containing water at normal density:

$$4\pi\rho_1 r_1^3 \int_0^1 \chi \xi^2 \, d\xi = \frac{4\pi}{3} \rho_0 r_1^3 \tag{2.28}$$

or

$$\frac{B_0}{m+3} + \frac{B_1}{2m+5} + \frac{B_2}{3m+7} + \frac{B_3}{4m+9} = \frac{\rho_0}{3\rho_1}$$

The tenth condition is the relation given as Eq. 2.26. Introducing the polynomials in Eq. 2.27 into Eq. 2.26 yields, with the use of the abbreviation

$$6.5 b_j = \sum_{i=0}^{j} \frac{B_i}{j+i} \qquad j = 1, 2, 3, \ldots, \tag{2.29}$$

the following relation for A_0:

$$\begin{aligned} A_0 = 1 &+ \frac{\rho_1 - \rho_0}{\rho_0} L_1 \left[C_0(b_1 - 2b_2 + b_3) + (14 - \varphi_1') \frac{b_2 - b_3}{6.5} + b_3 \right] \\ &- \frac{\rho_1}{\rho_0} \left[C_0(b_1 - 2b_2 + b_3) + (14 - \varphi_1') \frac{b_2 - b_3}{6.5} + b_3 \right] \\ &+ \frac{\rho_1 - \rho_0}{\rho_0} \left[C_0^2 b_1 + 8.5 C_0 C_1 b_2 + (7.5 C_1^2 + 15 C_0 C_2) b_3 + 21.5 C_1 C_2 b_4 + 14 C_2^2 b_5 \right] \\ &+ \frac{\rho_1 - \rho_0}{\rho_0} G_1 \left[\frac{dC_0}{d \ln \rho_1} (b_1 - 2b_2 + b_3) - \frac{d\varphi_1'}{d \ln \rho_1} \left(\frac{b_2 - b_3}{6.5} \right) \right]. \end{aligned} \tag{2.30}$$

This is an ordinary differential equation for C_0 as a function of ρ_1. Thus we have three simultaneous ordinary differential equations which determine A_0, B_0, and C_0, namely, Eqs. 2.23, 2.24, and 2.30. The other coefficients are given as follows:

$$\begin{aligned} A_1 &= 2 - 2A_0 - \varphi_1'/6.5 \\ A_2 &= 1 - A_0 - A_1 \\ B_1 &= -5.6 B_0 + \frac{30.568}{\rho_1} - 7.3728 + 0.1657 \chi_1' \\ B_2 &= 8.2 B_0 - \frac{31.136}{\rho_1} + 18.4379 - 0.4852 \chi_1' \\ B_3 &= -3.6 B_0 + \frac{30.568}{\rho_1} - 10.0651 + 0.3195 \chi_1' \\ C_1 &= \frac{14}{6.5} - 2C_0 - \varphi_1'/6.5 \\ C_2 &= 1 - C_0 - C_1. \end{aligned} \tag{2.31}$$

The accuracy of these polynomials has been tested for the Taylor case, where the exact solution is known. There was agreement up to the third decimal place, which showed that it is not necessary to include any more terms in the polynomials. This seemed particularly justified in view of the fact that we are not so much interested in the reduced functions φ, χ, and ψ as in the integral η_1 formed from them. Small inaccuracies or approximations used under such an integral usually have only a minor influence on the accuracy of the final result.

2.8 DETERMINATION OF β

In all relations derived so far, β, defined by Eq. 2.14, occurs as an unknown function of ρ_1. Only those φ's, χ's, and ψ's which involve a β satisfying equation, Eq. 2.14, are solutions of our problem.

The method used in this project determines β by means of an interpolation. First some arbitrary and constant values are assumed for β. Then φ, χ, and ψ are determined by the methods described above. Subsequently, η_1 is calculated using Eq. 2.3. When $\ln \eta_1$ is plotted vs $\ln (\rho_1 - \rho_0)/\rho_0$, the inclination of the η_1 curve we seek must have the value of β which was used to calculate this curve. Such a curve is readily found in the same way as the graphical solution of differential equations by the method of isoclines. Figure 2.2 illustrates the procedure.

Since it turned out that η_1 was not sensitive to the value assumed for β, an interesting conclusion may be made on the nature of the solution. If η_1 were assumed to be entirely independent of the assumed value of β, Eq. 2.14 would not be needed at all to arrive at a solution, and this would eliminate the arbitrary integration constant of this differential equation, i.e., we would have a singular solution, independent of the initial condition. It appears that this situation is approximately true for the solutions we have obtained. It therefore seems possible to start the calculation with different initial Taylor distributions, i.e., with different values of γ^0, such as 1.4, 1.66, or 7, and still obtain almost the same result for the shock-wave parameters at distances where pressure measurements can be made.

2.9 LOW-PRESSURE RANGE

When the shock front has propagated to large distances and the pressure is low, the wave behaves nearly like an acoustic wave. The peak pressure of such waves decreases approximately proportionally to the distance. For instance, Kirkwood and Bethe[9] have found the following asymptotic behavior of the weak shock waves:

$$p_1 \sim \frac{r_0}{r_1} \frac{c}{(\ln r_1/r_0)^{1/2}}, \tag{2.32}$$

where c is a constant and r_0 is the reference radius. From this we obtain

$$-\frac{d \ln p_1}{d \ln r_1} = 1 + \frac{1}{2} \frac{1}{\ln r_1/r_0}. \tag{2.33}$$

This magnitude approaches unity slowly as the shock-front distance increases to infinity.

Going back to Eq. 2.10, we find

$$\frac{d \ln p_1}{d \ln r_1} = \frac{U}{u_1} H_1 = \frac{-3}{1 + \frac{1}{\gamma_{RH}} \frac{\rho_1}{\rho_1 - \rho_0} (1 + \beta)} \tag{2.34}$$

or for low pressure, with the use of the approximation, Eq. 1.38,

$$-\lim_{p_1 \to p_0} \frac{d \ln p_1}{d \ln r_1} = 1 + \frac{1 - \beta}{3} + \ldots \tag{2.35}$$

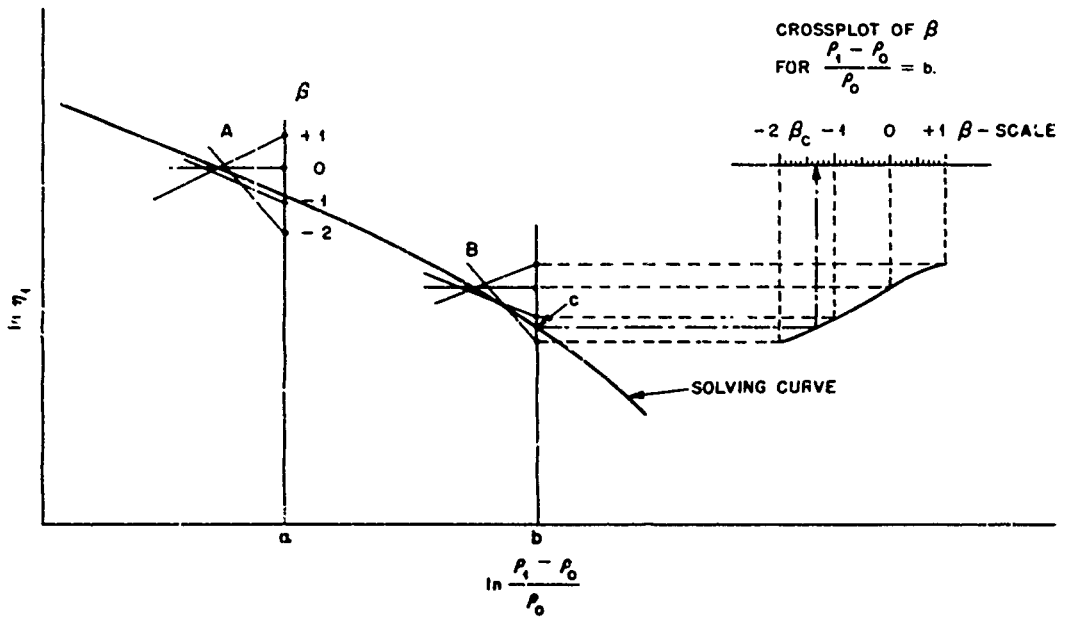

Fig. 2.2—Determination of $\beta = \frac{d \ln \eta_1}{d \ln (\rho_1 - \rho_0)/\rho_0}$

For each value of ρ_1 several values of β are assumed, such as $\beta = +1, 0, -1, -2$, etc. For each of these values of β, η_1 is calculated using Eq. 2.3, and ln η_1 is plotted vs ln $(\rho_1 - \rho_0)/\rho_0$. The correct β is the slope of the solving curve in this plot. The solving curve is obtained by interpolation among the calculated data. Examples of these data for two values of ρ_1 are shown at a and b. As a first approximation, a curve is drawn from the known initial value of η_1 at $\rho_1 = 4\rho_0$ through the regions of intersections A and B. The approximate curve is then adjusted at each ρ_1, until the slope of the curve is equal to the interpolated value of β. This interpolation is readily accomplished with the aid of a crossplot such as the one shown. For example, the inclination of the solving curve at the point c must be equal to β_c read from the β scale of the crossplot.

Comparison of Eqs. 2.35 and 2.33 shows that, for low pressure, β must slowly approach unity. From the definition of β, Eq. 2.14, it can be seen that η_1 must tend to zero. This gives us qualitative information on φ and ψ: they must tend to vanish for most values of ξ for very low shock pressures, or else the integral for η_1, Eq. 2.3, could not become zero. χ does not vanish, as can be seen from the average density condition, Eq. 2.28; in fact, χ approaches unity when $\rho_1 \to \rho_3$.

Since

$$\left.\begin{matrix}\varphi \to 1\\ \psi \to 1\end{matrix}\right\} \quad \text{for} \quad \xi \to 1$$

and

$$\chi = 0 \quad \text{for} \quad \xi = 0,$$

we obtain in the limit for zero shock pressure:

$$\lim_{\rho_1 \to \rho_0} \varphi = \lim_{\rho_1 \to \rho_0} \psi = 0 \qquad 0 \le \xi < 1$$

$$\lim_{\rho_1 \to \rho_0} \chi = 1 \qquad 0 < \xi \le 1.$$

There is a discontinuous drop of φ and ψ from 1 to 0 at $\xi = 1$ and also for χ at $\xi = 0$.

This implies that the derivatives φ_1' and ψ_1' increase to infinity when $\rho_1 \to \rho_0$, but χ_1' vanishes. Indeed, Eqs. 2.16 to 2.18 become, with the use of Eqs. 1.38 and 1.39,

$$\lim_{\rho_1 \to \rho_0} \varphi_1' = \lim_{\rho_1 \to \rho_0} \psi_1' = -\frac{2\rho_0}{\rho_1 - \rho_0} \frac{1}{a_2} \frac{1-\beta}{2+\beta},$$

$$\lim_{\rho_1 \to \rho_0} \chi_1' = -\frac{2}{a_2} \frac{1-\beta}{2+\beta} \to 0. \tag{2.36}$$

Thus $(1-\beta)/(\rho_1 - \rho_3)$ approaches ∞ as ρ_1 approaches ρ_0. It is difficult to evaluate the integral η_1 for these conditions, because J increases rapidly with decreasing ξ for low values of ρ_1. Basically, this is because the bubble and shock-wave phenomena become spatially separated. Most of the shock-wave energy is concentrated near the shock front and can be easily accounted for by the methods described above. But this is only a fraction of the total energy, since an appreciable amount of energy is found as internal energy near the center. This latter energy produces the phenomena of the pulsating bubble and is not conveniently accounted for by the method described in Secs. 2.7 and 2.8.

Therefore, to obtain η_1, we may calculate the shock-wave energy and try to find a relation between total energy and shock-wave energy.

At the shock front, energy is dissipated because of the irreversible shock process and is converted into thermal energy. The shock-wave energy Q_S is reduced correspondingly. Kirkwood and Brinkley, Eq. 4.29 in reference 14, have formulated this phenomenon as follows:

$$\frac{dQ_S}{dr_1} = -4\pi\rho_0 h r_1^2, \tag{2.37}$$

where $Q_S = 4\pi \int_{t(r_1)}^{\infty} [r(t)]^2 u\rho\, dt$ and h = dissipated enthalpy increment. The integral for the shock-wave energy has to be carried along the path of the fluid particle which is reached by the shock front at $t = t(r_1)$ and $r = r_1$. The upper limit corresponds to a long time compared with the duration of the shock wave but must be chosen in such a way that secondary pulses are not included.

In NAVORD Report 4182 the shock-wave energy Q_S is expressed by a volume integral. Defining the reduced shock-wave energy η_S in the same way as the reduced total energy, the following expressions have been found

$$Q_S = \frac{4}{3}\pi r_1^3 p_1 \frac{\rho_1 - \rho_0}{2\rho_0}\eta_S \tag{2.38}$$

and

$$\lim_{\rho_1 \to \rho_0} \eta_S = 3\int_0^1 (\varphi^2\chi + \psi^2)\,\xi^2\,d\xi \tag{2.39}$$

$$= \frac{3}{2\varphi_1' + \chi_1' + 3} + \frac{3}{2\psi_1' + 3}, \tag{2.39a}$$

where the derivation of Eq. 2.39a is explained in NAVORD Report 4182. With Eq. 2.36, this becomes

$$\lim_{\rho_1 \to \rho_0} \eta_S = \frac{3}{2} a_2 \frac{\rho_1 - \rho_0}{\rho_0}\frac{2+\beta}{1-\beta}. \tag{2.40}$$

This equation is of little help yet, since it relates the reduced shock-wave energy with β, the derivative of the reduced total energy. Another expression for η_S can be obtained from Eq. 2.37. Introducing Eq. 2.38 yields after a few manipulations

$$\eta_S = \frac{2h\rho_0^2}{p_1(\rho_1 - \rho_0)} \frac{1 + \frac{1}{\gamma_{RH}}\frac{\rho_1}{\rho_1 - \rho_0}(1+\beta)}{\frac{1}{\gamma_{RH}}\frac{\rho_1}{\rho_1 - \rho_0}(\beta_S - \beta)} \tag{2.41}$$

and, with the use of Eqs. 1.38, 1.39, and 1.41,

$$\lim_{\rho_1 \to \rho_0} \eta_S = \frac{a_2}{3}\frac{\rho_1 - \rho_0}{\rho_0}\frac{2+\beta}{\beta_S - \beta}, \tag{2.42}$$

where

$$\beta_S = \frac{d \ln \eta_S}{d \ln \frac{\rho_1 - \rho_0}{\rho_0}}.$$

Combination of Eqs. 2.40 and 2.42 gives the following differential equation for η_S (the limit sign is omitted):

$$\eta_S = \frac{3a_2}{2}\frac{\rho_1 - \rho_0}{\rho_0}\frac{(4/3) + \beta_S}{1 - \beta_S}. \tag{2.43}$$

Its solution is

$$\eta_S = \frac{3a_2}{2}\frac{\rho_1 - \rho_0}{\rho_0}\left(\frac{7}{3}\ln\frac{C\rho_0}{\rho_1 - \rho_0} - \ln\frac{\rho_0\eta_S}{\rho_1 - \rho_0}\right), \tag{2.43a}$$

where C is the integration constant. Combination of this solution with Eq. 2.40 yields the desired asymptotic expression for β:

$$\lim_{\rho_1 \to \rho_0} \beta = 1 - \frac{3}{1+\varkappa} \qquad \varkappa C^{\varkappa} = \left(\frac{C\rho_0}{\rho_1 - \rho_0}\right)^{7/3}. \tag{2.44}$$

The merit of this simple expression is that it shows how β can be extended into the low-pressure region where the calculation of η_1 becomes inconvenient. The integration constant c is determined by the results for β obtained in the high-pressure region; β must merge smoothly from one region into the other.

2.10 PEAK APPROXIMATION

Another, more elaborate, treatment of the low-pressure range is done by the use of the peak approximation. By "peak approximation" we refer to the attempts of various authors to describe the shock-wave propagation in terms of shock parameters only. This can be done by making certain idealizing assumptions, for instance, assuming a similarity restraint on the wave shape. Kirkwood and Bethe as well as Kirkwood and Brinkley have presented such shock-wave theories, and in their application to underwater explosions they assumed an exponential wave shape. These theories have been successful, and they would be quite appropriate for our case. We have used the more recent theory by Snay and Matthias.[1]

The Snay-Matthias theory gives an interrelation between peak pressure, time constant, and the profile of the wave which is characterized by the shape factor i. This magnitude is defined as follows:

$$i = \left[\frac{p(\partial^2 p/\partial t^2)}{(\partial p/\partial t)^2}\right]_{r=r_1}, \tag{2.45}$$

where f is unity for an exponential wave shape and zero for a triangular wave shape. The theory leads to the following differential equations:*

$$\frac{dp_1}{dx} + \frac{P_{11}}{x} + P_{12}\alpha = 0 \tag{2.46}$$

$$\frac{d\alpha}{dx} + \frac{P_{13}}{x^2} + \frac{P_{14}\alpha}{x} + P_{15}\alpha^2(1 + fP_{16}) = 0 \tag{2.47}$$

where x = reduced distance = r_1/r_0
r_0 = reference length (will cancel in this analysis)
α = time factor = $r_0/\theta c_0$
θ = time constant = $-p/(\partial p/\partial t)$
c_0 = sound velocity at $p = 0$

The variable coefficients P_i of these differential equations are obtained from the three hydrodynamic partial differential equations and are functions of the peak pressure p_1 only.

Introducing β and ρ_1, these two equations can be transformed, with the use of Eqs. 2.34 and 1.12, to:

$$\beta = \frac{3}{w_1 + w_2\alpha x} - \gamma_{RH}\frac{\rho_1 - \rho_0}{\rho_1} - 1 \tag{2.48}$$

and

$$\frac{d \ln \alpha x}{d \ln \frac{\rho_1 - \rho_0}{\rho_0}} = \frac{-1}{w_1 + w_2\alpha x}\left(w_3 - \frac{w_4}{\alpha x} - w_5\alpha x - w_6 f\alpha x\right), \tag{2.49}$$

*See reference 1, Eqs. 1.6 and 2.7, where the symbol α_1/a^2 instead of f is used to designate the shape factor.

where $w_1 = \frac{1}{\gamma_{RH}} \frac{\rho_1}{\rho_1 - \rho_0} \frac{P_{11}}{P_1}$

$w_2 = \frac{1}{\gamma_{RH}} \frac{\rho_1}{\rho_1 - \rho_0} \frac{P_{12}}{P_1}$

$w_3 = 1 - P_{14}$

$w_4 = P_{13}$

$w_5 = P_{15}$

$w_6 = P_{15}P_{16}$

and

$$\sigma x = \frac{r_1}{c_0 \theta}. \tag{2.50}$$

The variable coefficients w_i are listed in Table 2.1. They are now functions of ρ_1.

Table 2.1 — VARIABLE COEFFICIENTS OF EQS. 2.48, 2.49, AND 2.56

ρ_1/ρ_0	w_1	w_2	w_3	w_4	w_5	w_6
1.60	0.3523	0.0375	1.311	4.45	−0.0187	0.098
1.50	0.3917	0.0468	1.262	3.32	−0.0182	0.114
1.40	0.4578	0.0607	1.240	2.33	−0.0158	0.128
1.30	0.5182	0.0756	1.190	1.50	0.0000	0.140
1.20	0.5874	0.0877	1.124	0.810	0.0300	0.142
1.15	0.6434	0.0931	1.092	0.533	0.0750	0.129
1.10	0.7326	0.0921	1.067	0.312	0.0813	0.110
1.075	0.8005	0.0820	1.052	0.220	0.0770	0.0952
1.050	0.8769	0.0634	1.038	0.143	0.0585	0.0753
1.040	0.8980	0.0544	1.032	0.112	0.0508	0.0642
1.030	0.9281	0.0420	1.024	0.0830	0.0420	0.0511
1.020	0.9501	0.0298	1.0172	0.0535	0.0309	0.0356
1.010	0.9744	0.0159	1.0085	0.0255	0.0175	0.0196
1.005	0.9858	0.0087	1.0042	0.0122	0.0095	0.0097

Equations 2.48 and 2.49 would yield β as a function of $(\rho_1 - \rho_0)/\rho_0$, if the shape factor f were known as a function of ρ_1. In the high-pressure region, however, we have already determined β as described above. Here Eqs. 2.48 and 2.49 can be used to calculate the shape factor. The result is shown in Fig. 2.4. Also, for the low-pressure range, the asymptotic relations in Eq. 2.44 can be used to find the shape factor. The value of f in the intermediate range can then be approximated by interpolation.

In the actual calculations, we used a combination of the two methods described above. First, the integration constant c in the asymptotic expression, Eq. 2.44, was approximately determined by merging the two parts of the β curve graphically, as shown in Fig. 2.3. Once this integration constant is known, the shape factor can be calculated for the low pressures and interpolated in the intermediate range. Now Eqs. 2.48 and 2.49 can be used to find β and, subsequently, an improved integration constant c. The procedure is repeated until satisfactory convergence is obtained. It turns out that the shape factor has a maximum and a minimum in the range of our interest and varies between 1.65 and 0.53 (see Fig. 2.4). These calculations yield β over the entire range of our project. Subsequently η_1 can be determined by integration. This concludes the major part of the shock-wave calculations since now the peak pressure–

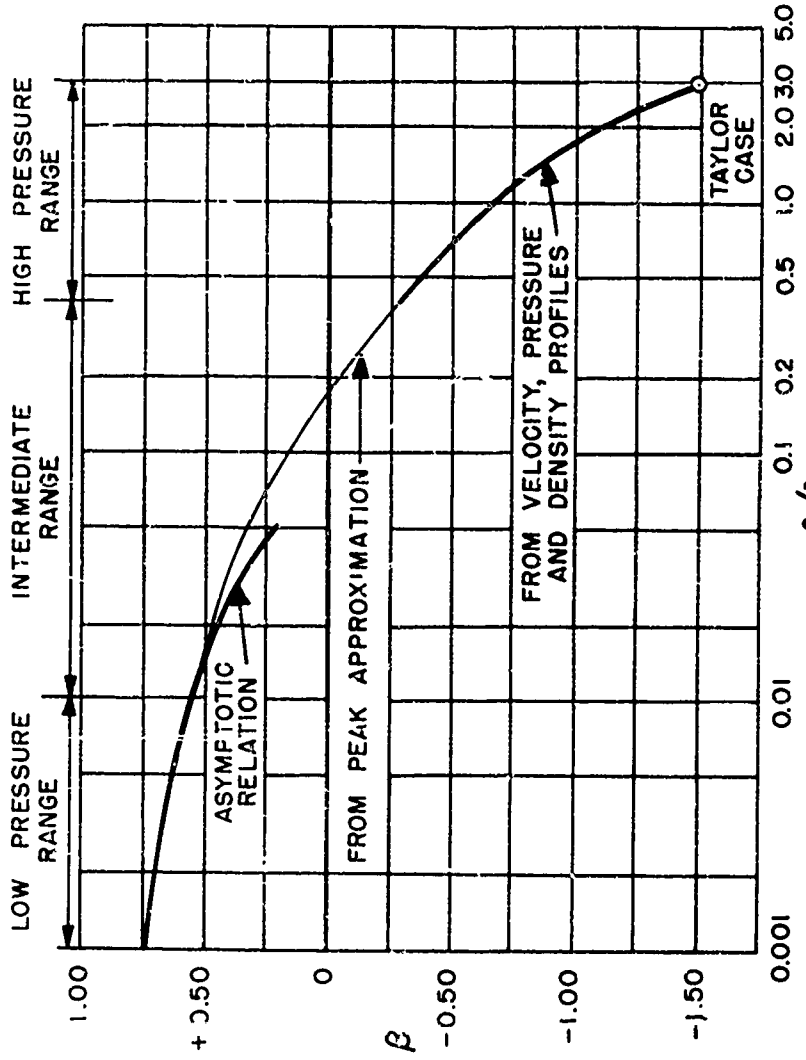

Fig. 2.3—β for the entire pressure range.

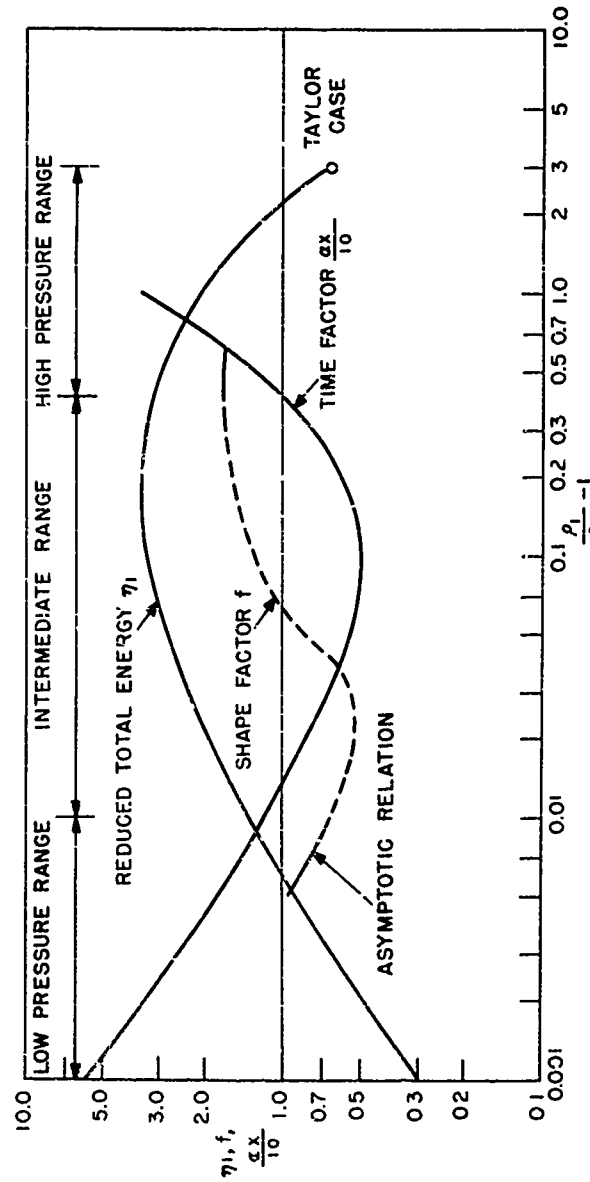

Fig. 2.4—Shape factor, reduced total energy, and time factor.

distance curve as well as other shock parameters can be readily computed, as will be described in the next section.

2.11 SUMMARY AND RESULTS

For the benefit of the reader who is less interested in mathematical developments, the salient points of the analysis are summarized here.

The main objective is to calculate the shock-wave peak pressure as a function of distance for a point explosion. A convenient expression for the pressure-distance relation may be obtained from the fact that the total energy of the spherical disturbance caused by the explosion must be constant and equal to Q, the hydrodynamic yield of the explosion. The mathematical expression of this statement is

$$Q = \frac{4}{3}\pi r_1^3 p_1 \frac{\rho_1 - \rho_0}{2\rho_0}\eta_1 = \text{constant}, \tag{2.51}$$

where p_1 = shock-wave peak pressure
ρ_1 = peak density
ρ_0 = density of the undisturbed water
r_1 = distance of the shock front from the center of the explosion
η_1 = reduced total energy as defined below (see Eq. 2.53)

According to the Rankine-Hugoniot conditions, the shock pressure p_1 is a function of ρ_1/ρ_0 and is given by the Rankine-Hugoniot adiabatic, Eq. 1.1. In the thermodynamic part of the calculations this function has been numerically determined and is presented in Table 3.1. It will be noted that ρ_1 varies between $4\rho_0$ and ρ_0. The latter value corresponds to $p_1 = 0$; the first, to $p_1 = \infty$; hence to the instant of explosion: $t = 0$ and $r_1 = 0$.

It was found advantageous in the analysis to use the magnitude ρ_1/ρ_0 as the principal independent variable. (For simplicity, we write ρ_1 instead of the above ratio, assuming ρ_0 is a constant and known magnitude.) A glance at Table 3.1 will show that it is possible, once ρ_1 is specified, to determine any other variable of interest, such as pressure, radius, or time.

The reduced total energy η_1 depends on the shock strength; hence

$$\eta_1 = \eta_1(\rho_1). \tag{2.52}$$

Once this relation between η_1 and ρ_1 is found, the corresponding distance of the shock front r_1 is easily found from the energy equation, Eq. 2.51.

η_1 is defined by

$$\eta_1 = 3\int_{r_1=0}^{r_1=r_1}\left[\left(\frac{u}{u_1}\right)^2\frac{\rho}{\rho_1} + \frac{2J\rho_0}{\rho_1-\rho_0}\frac{p}{p_1}\right]\left(\frac{r}{r_1}\right)^2 d\left(\frac{r}{r_1}\right)$$

$$= 3\int_0^1\left(\varphi^2\chi + \frac{2J\rho_0}{\rho_1-\rho_0}\psi\right)\xi^2\,d\xi \tag{2.53}$$

where u_1 is the particle velocity directly behind the shock front; the symbols without subscripts refer to points between the front and the center; φ is the reduced velocity, χ is the reduced density; ψ is the reduced pressure; and ξ is the reduced distance. These reduced variables take values only between zero and unity. Figure 2.1 shows the behavior of these magnitudes for various values of ρ_1. J is the reduced internal energy discussed in Sec. 1.2. It is a function of three variables, namely, ρ_1, ψ, and χ. These data are directly obtained by the thermodynamic calculations outlined in Chap. 1 and are shown in Fig. 1.4. Obviously the material presented in Figs. 1.4 and 2.1 provides all the information necessary to calculate η_1 by means of Eq. 2.53. However, to obtain φ, χ, and ψ as functions of ξ and ρ_1, one must solve

the three partial differential equations of the fluid motion. In NAVORD Report 4164 several methods are proposed which provide approximate solutions of reasonable accuracy.

One of the interesting features is that simple equations exist for the inclination of the φ, χ, and ψ curves at $\xi = 1$ (Eqs. 2.16 to 2.18). This means that the behavior of the reduced variables near $\xi = 1$ can be found in a relatively simple manner, which is most important for the finding of η_1 by means of the integral, Eq. 2.53. Since the factor ξ^2 occurs in the integrand, values for small ξ contribute little to the total value of the integral and hence do not need to be known precisely. (This holds for high pressures only. In the intermediate- and low-pressure ranges J increases rapidly with decreasing ξ. Hence, other methods are used in these ranges.) For greater accuracy in the evaluation of η_1 in the high-pressure range, we have derived series for the reduced variables which describe their behavior around $\xi = 0$. Combination of both treatments by means of polynomials, which incorporate the information available at $\xi = 0$ as well as at $\xi = 1$, resulted in the expressions in Eq. 2.27. Their accuracy is excellent in the one instance where a comparison with the rigorous solution was possible.

However, there is one difficulty in these otherwise simple calculations; they involve* an unknown parameter, namely,

$$\beta = \frac{\rho_1 - \rho_0}{\rho_0 \eta_1} \frac{d\eta_1}{d\frac{\rho_1}{\rho_0}} = \frac{d \ln \eta_1}{d \ln \frac{\rho_1 - \rho_0}{\rho_0}} . \tag{2.54}$$

This magnitude is the inclination of the η_1 curve, when plotted vs $(\rho_1 - \rho_0)/\rho_0$ in a logarithmic scale. Figure 2.2 shows such a plot.

Actually β is the magnitude of principal concern, because, once $\beta(\rho_1)$ is known, the important magnitude η_1 can be readily obtained by integration. Therefore the greatest part of the analysis is devoted to the task of finding β. A different method was used in each of the three pressure regions considered.

The high-pressure region corresponds to ρ_1 between $4\rho_0$ and $1.4\rho_0$ and to pressures between ∞ and 484,000 psi. Here, η_1 was calculated from Eq. 2.53 with various arbitrarily assumed values of β. Then η_1 is plotted vs $(\rho_1 - \rho_0)/\rho_0$ and an η_1 curve is constructed which has an inclination equal to the assumed β. Along this curve the condition in Eq. 2.54 is satisfied, and this β is the solution of our problem. The interpolation method used to select β is illustrated in Fig. 2.2.

The low-pressure region extends from $\rho_1 = 1.01\rho_0$ down to $\rho_1 = \rho_0$ and corresponds to pressures between 3260 psi and zero. For this region, the following asymptotic relation can be derived:

$$\beta = 1 - \frac{3}{1 + \varkappa} ; \qquad \varkappa e^{\varkappa} = \left(\frac{c\rho_0}{\rho_1 - \rho_0} \right)^{1/3} \tag{2.55}$$

This determines β as a function of ρ_1 and an integration constant c which is to be determined. Figure 2.3 shows the form of the β curve when plotted vs the logarithm of $(\rho_1 - \rho_0)/\rho_0$. A change of c moves this curve horizontally either to the left or to the right without changing the ordinates. This shows how the β curve can be approximately drawn for both the low-pressure and the intermediate-pressure ranges: The asymptotic pressure curve is moved into such a position that a smooth curve is obtained from the high-pressure down to the low-pressure range. The curve thus obtained corresponds to the fine line in Fig. 2.3. (The figure actually shows not this crude intermediate approximation but the final result obtained with the use of the subsequently described method.)

The intermediate-pressure range has been calculated by means of a "peak approximation." With this term, we refer to the theories in which an attempt is made to describe the shock-wave propagation in terms of shock parameters, such as peak pressure, time constant, or re-

*Compare Eqs. 2.16 to 2.18, 2.10, and 2.14 of this report.

lated magnitudes. This is only possible if assumptions as to the shape of the wave profile are made, and they are approximations for that reason. Examples are the highly successful Kirkwood-Bethe and Kirkwood-Brinkley theories. We have used in this project the more recent theory of Snay and Matthias.[1] Adapted to our problem, this theory yields:

$$\beta = \frac{3}{w_1 + w_2\alpha x} - 1 \qquad RH \frac{\rho_1 - \rho_0}{\rho_1} - 1$$

$$\frac{d \ln \alpha x}{d \ln \frac{\rho_1 - \rho_0}{\rho_0}} = \frac{-1}{w_1 + w_2\alpha x}\left(w_3 - \frac{w_4}{\alpha x} - w_5\alpha x - w_6 f \overline{\alpha x}\right), \tag{2.56}$$

where w_1 to w_5 - functions of ρ_1, listed in Table 2.1

αx = time factor = $r_1/c_0\theta$

c_0 = sound velocity at $p_1 = 0$

θ = time constant = $p \div (\partial p/\partial t)$

f = shape factor, see Eq. 2.45 (f is unity for an exponential wave, zero for a triangular wave)

γ_{n11} = $(d \ln p_1)/(d \ln \rho_1)$, listed in Table 3.1.

At the end of the high-pressure range, $\rho_1/\rho_0 = 1.4$, we know all three magnitudes involved in Eqs. 2.56, namely β, αx, and f. The latter two are the initial conditions for the above differential equation. To integrate this equation, f must be known as a function of ρ_1. Assumption of a constant f would have been a good approximation. We went even further by estimating f as a function of ρ_1, as described in Sec. 2.10 and shown in Fig. 2.4. Finally, integration of Eqs. 2.56 yields β as well as αx from which the time constant θ can be obtained. The results are given in Table 3.1.

Subsequent straightforward calculations yield η_1, Eq. 2.54, and the shock-front distance r_1, Eq. 2.51. This yields the desired pressure-distance relation. The other shock-wave parameters, such as time constant and shock-wave energy, can now be calculated without difficulty. This will be explained in the following paragraphs, together with the presentation of the numerical results.

The peak pressure–distance curve for a point explosion with a yield of 30 kt of TNT is presented in Fig. 2.5 together with the experimental evidence obtained in Operation Wigwam, as given in the preliminary version of reference 15. Also shown are the results of the preliminary calculations submitted prior to the test as "predictions." The two curves differ in the range of interest by very minor amounts, and either one is in good agreement with the experimental results.

The pressure-distance relation for any other yield Q can be easily calculated from the values of $r_1/Q^{1/3}$ which, together with the peak pressure, are given in Table 3.1. For low pressures (3000 psi and below), this relation can be approximated as follows:

$$p_1 = 4.608 \times 10^6 \left(\frac{Q^{1/3}}{r_1}\right)^{1.13} \tag{2.57a}$$

$$= 18{,}800 \left(\frac{W^{1/3}}{r_1}\right)^{1.13}, \tag{2.57b}$$

where p_1 is in pounds per square inch; r_1 is in feet; Q is in kilotons of TNT, where 1 kt is 10^{12} g-cal ($\sim 4.20 \times 10^{19}$ ergs); and W is in pounds of TNT (1 kt = 2.205×10^6 lb).* Comparison of

*A detonation energy of 10^3 cal/g has been assumed for TNT. Previously published values which are up to 10 per cent higher than this are based on theoretical calculations which are superseded today. A reliable value is not known, and there are indications that even 10^3 cal/g is too high. This shows clearly that the choice of kilotons of TNT as an energy unit is an unfortunate one.

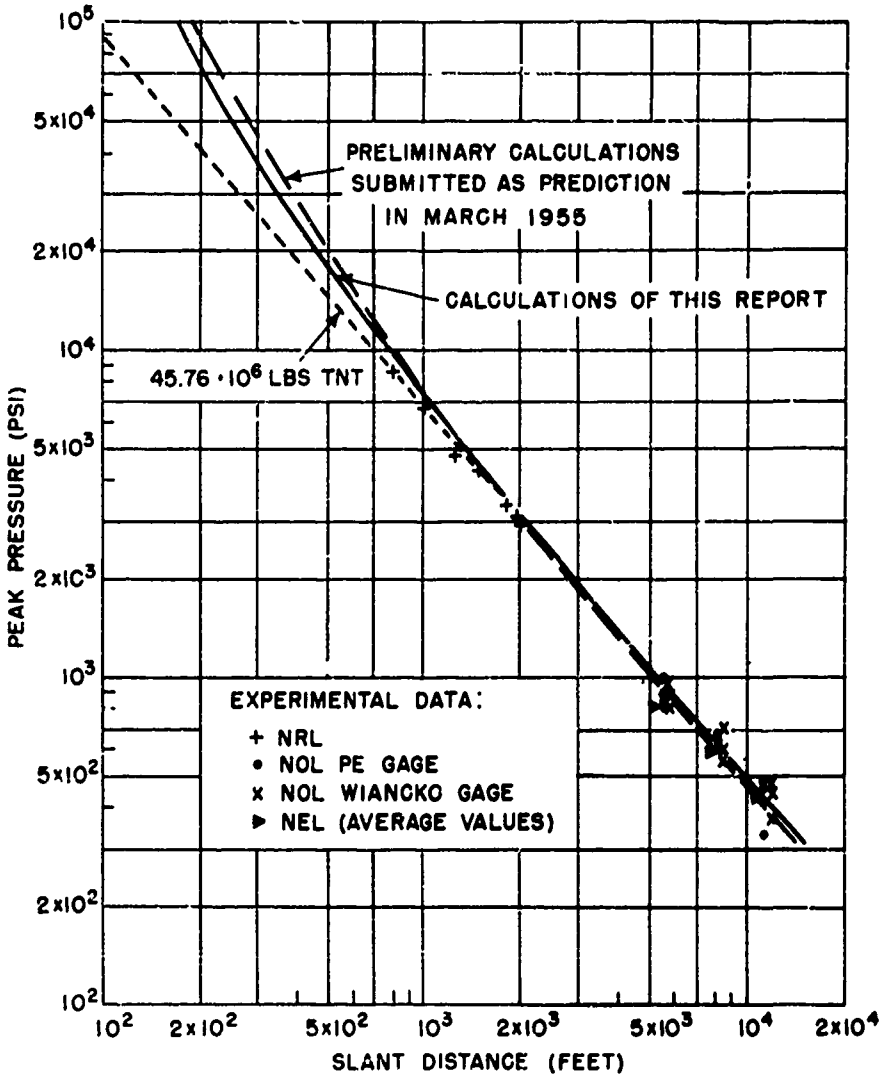

Fig. 2.5—Peak pressure vs distance.

Eq. 2.57b with the corresponding formula for the shock-wave peak pressure produced by a TNT explosion,

$$p_1 = 21{,}600 \left(\frac{W^{1/3}}{r_1}\right)^{1.13}, \tag{2.58}$$

shows that for a point explosion an energy equivalent to that of 1.446 lb of TNT is necessary to produce the same shock pressure as does 1 lb of exploding TNT. Or, in other words, the shock-wave peak pressure of a point explosion with a yield of 1 kt of TNT is equal to that of an exploding 0.692-kt TNT charge.

The shock-wave peak pressures observed at Wigwam correspond to those produced by a TNT explosion of 46.2×10^6 lb charge weight.[16] The actual yield of the Wigwam explosion is not accurately known. The following values were quoted at the Wigwam Project Officers' Conference at the Naval Radiological Defense Laboratory, San Francisco, in October 1955:

Radiochemical yield:
Los Alamos Scientific Laboratory, 32 ± 3.2 kt of TNT
Naval Research Laboratory, 35 – 2.5 + 10 kt of TNT
Hydrodynamic yield:
Armour Research Foundation, 30.5 ± 1 kt of TNT.

Using the LASL value, it is found that according to the experimental evidence of Operation Wigwam, an atomic underwater explosion with a yield of 1 kt of TNT would produce the same shock-wave peak pressure as a TNT explosion of 0.65 ± 0.12 kt charge weight. The calculated value (0.692 kt) is within the limits of the experimental error. This error appears to be large, because expressing the shock-wave peak pressure in terms of energy amplifies the errors of the pressure measurements by the power 3/1.13 = 2.655. For the same reason it is more difficult to predict accurately the energy equivalent than the shock-wave pressure.

If the calculated curves in Fig. 2.5 were drawn for a yield of 32 kt of TNT instead of 30 kt of TNT, the pressures would be 2.5 per cent higher—a change which would hardly affect the agreement with the experimental points shown. Since the question of the actual yield was not settled at the time of this writing, all data in this report are presented for 30 kt of TNT, the yield for which the calculations were originally made.

The time constant is defined by

$$\theta = -\frac{p}{(\partial p/\partial t)_r} = \frac{r_1}{c_0}\frac{1}{\alpha x}. \tag{2.59}$$

Calculated numerical values of $\theta/Q^{1/3}$ as well as θ for 30 kt of TNT are listed in Table 3.1. Figure 2.6 shows a comparison with the test results: the calculated time constant is about 10 per cent too high. Since most shock-wave theories give poor results for the time constant, the agreement may be considered satisfactory.

The arrival time for the shock front at a point at a distance r_1 is given by

$$t = \int_0^{r_1} \frac{dr}{U}, \tag{2.60}$$

where U is the propagation velocity of the shock front

$$U = \left(\frac{p_1}{\rho_0}\frac{\rho_1}{\rho_1 - \rho_0}\right)^{1/2}. \tag{2.61}$$

Introduction of the variables β and η_1 yields

$$t = \frac{Q^{1/3}}{3(\rho_0)^{1/2}}\frac{1}{(4/3\pi)^{1/3}}\int_{\rho_1}^{4}\frac{1+\beta+\dfrac{\rho_1-\rho_0}{\rho_1}\gamma_{RH}}{\left(\dfrac{\rho_1-\rho_0}{\rho_0}\right)^{5/6}(\eta_1)^{1/3}(p_1)^{5/6}}\left(\frac{\rho_0}{\rho_1}\right)^{1/2}d\rho_1. \tag{2.62}$$

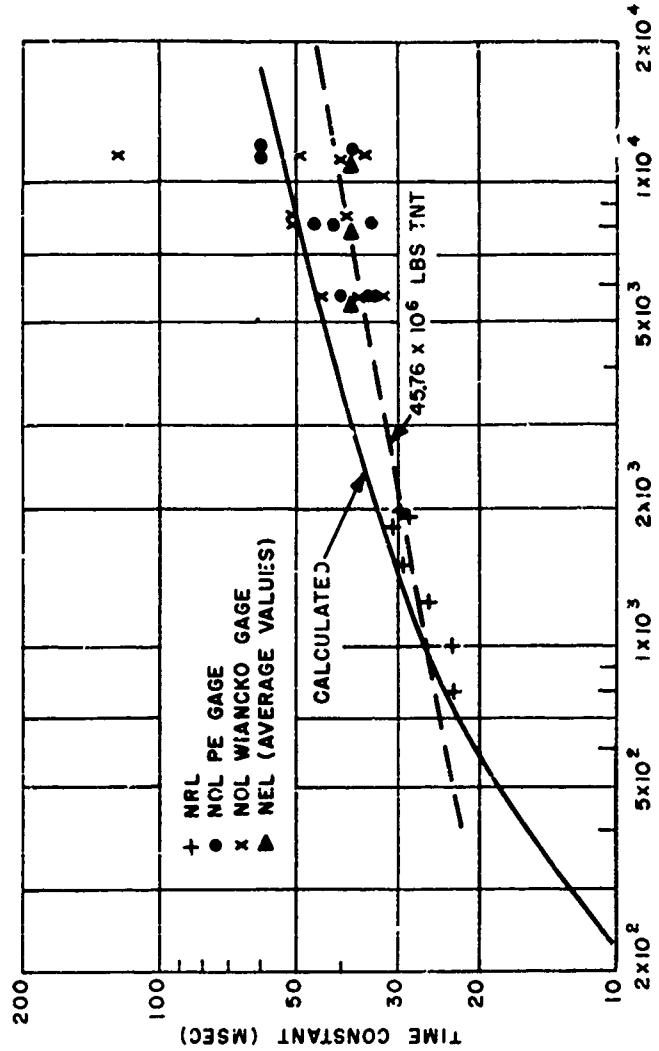

Fig. 2.6—Time constant vs distance.

Numerical results for t as well as t $Q^{1/3}$ are given in Table 3.1. For high pressures and small distances, the arrival time can be obtained by means of the Taylor solution (reference 13, Eqs. 7 and 8). In our notation,

$$t = \frac{2\sqrt{2}}{5\sqrt{3}} (\rho_1 - \rho_0) \left(\frac{\pi\eta_1}{\rho_1}\right)^{1/2} \frac{(r_1)^{5/2}}{Q^{1/2}}$$

$$= 5.588 \times 10^{-4} \frac{(r_1)^{5/2}}{Q^{1/2}} \tag{2.63}$$

$$= 0.830 \frac{(r_1)^{5/2}}{W^{1/2}},$$

where the numerical values apply to $\rho_1 = 4\rho_0$, t in milliseconds, Q in kilotons of TNT, W in pounds of TNT, and r_1 in feet.

For moderate and large distances Eq. 2.62 gives good agreement with the test results reported in the preliminary version of reference 16 (see Fig. 2.7). However, for close-in distances both Eqs. 2.62 and 2.63 are in poor agreement with the test results (Fig. 2.7). This disagreement is probably due to the idealizing assumption of a point explosion with an isentropic exponent of $\frac{5}{3}$. For real explosions this value may be higher.

The shock-wave energy flux (commonly called shock-wave energy) is, for low pressures,

$$\mathcal{E}_{SW} = \frac{1}{\rho_0 c_0} \int_0^\infty p^2 \, dt. \tag{2.64}$$

This magnitude is equivalent to the integral Q_S in Eq. 2.37 and can be expressed as follows:

$$E_{SW} = \frac{\eta_S}{\eta_1} \frac{Q^{1/3}}{4\pi} \left(\frac{Q^{1/3}}{r_1}\right)^2, \tag{2.65}$$

where η_S is the reduced shock-wave energy defined by Eq. 2.38. The ratio $(1/4\pi)(\eta_S/\eta_1)$ is listed in Table 3.1 It is a slowly varying function of ρ_1 or, what amounts to the same thing, of $Q^{1/3}/r_1$. For pressures below 3000 psi we have approximately

$$\frac{1}{4\pi} \frac{\eta_S}{\eta_1} = 2.15 \times 10^{-2} \left(\frac{Q^{1/3}}{r_1}\right)^{0.05}, \tag{2.66}$$

and, by combination with Eq. 2.65,

$$E_{SW} = 5.522 \times 10^9 \, Q^{1/3} \left(\frac{Q^{1/3}}{r_1}\right)^{2.05} \tag{2.67a}$$

$$= 1963 W^{1/3} \left(\frac{W^{1/3}}{r_1}\right)^{2.05}, \tag{2.67b}$$

where E_{SW} is in inch-pounds per square inch, r_1 is in feet, Q is in kilotons of TNT, and W is in pounds of TNT. It should be noted that these theoretical formulas apply to the total shock-wave energy. In the empirical formula for TNT,

$$E_{SW} = 2410 W^{1/3} \left(\frac{W^{1/3}}{r_1}\right)^{2.05}, \tag{2.68}$$

the integration in Eq. 2.64 is carried up to 6θ and not to infinity. However, for all practical purposes this is equivalent to the total shock-wave energy. The experimental values shown in Fig. 2.8 are obtained by integrating up to the time of the surface cutoff only; this occurred at

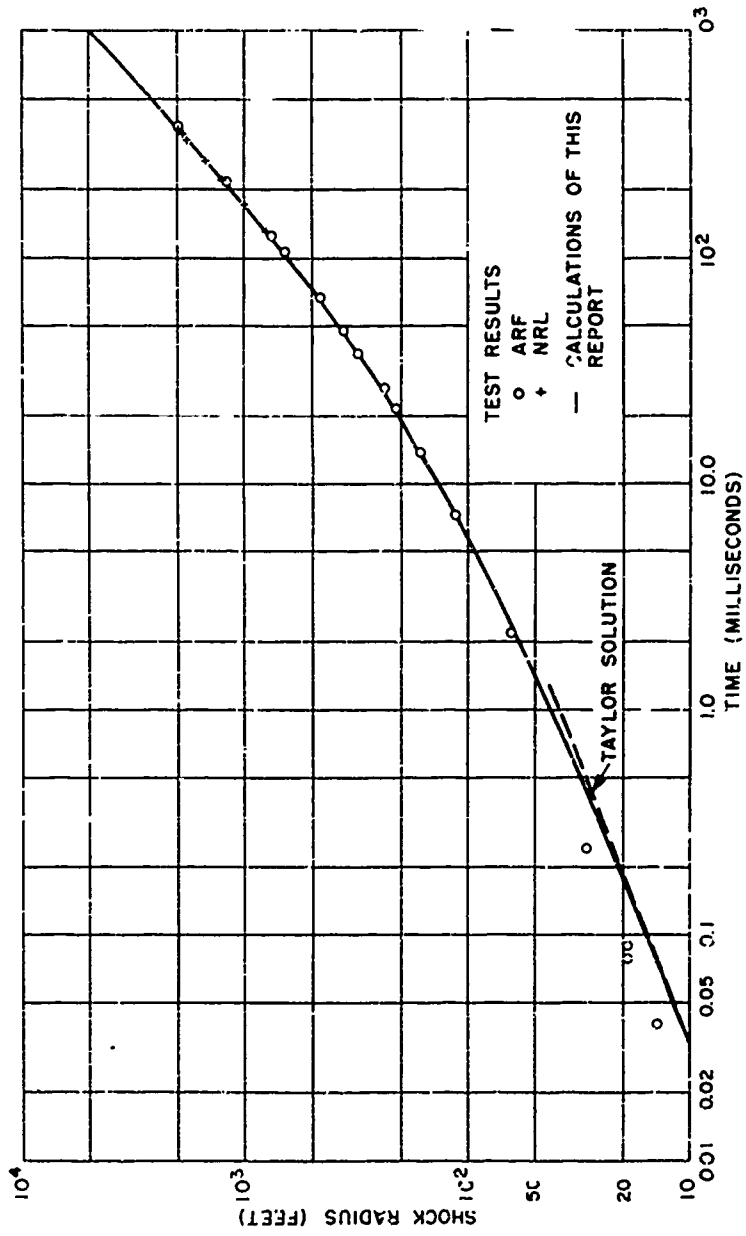

Fig. 2.7—Distance vs time of arrival.

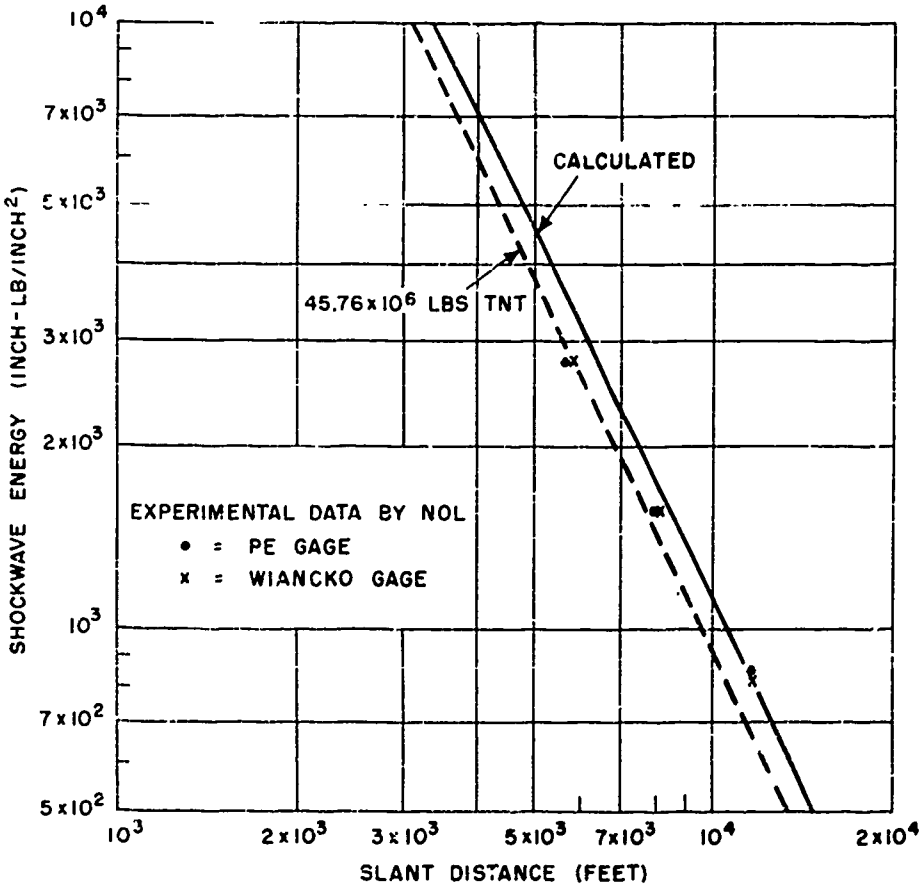

Fig. 2.8— Shock-wave energy vs distance.

about $t = 10$ to $t = 30$. They represent only fractions of the total energy, although very large fractions. Considering these factors of uncertainty, the agreement between theory and experiment is fairly good.

An explosion of 45.76×10^6 lb of TNT, which would give the same shock-wave peak pressure as a 30-kt TNT point explosion, would not produce the same shock-wave energy (see Fig. 2.8). An explosion of 54.06×10^6 lb of TNT would be necessary to do this, as can be found from Eqs. 2.68 and 2.67b.

CHAPTER 3

BUBBLE PHENOMENA

3.1 INTRODUCTION

The nature of the bubble formation by a point explosion differs in some respects from that of conventional explosives. In the latter case the reaction products of the explosion expand and push the water aside, thus forming a gas sphere which then performs the well-known bubble pulsations. The bubble interface always consists of the same particles, namely, those which were in contact with the charge before the explosion. Vaporization of the water is entirely unimportant.

In the case of a point explosion, the water is pushed aside by expanding steam. The heat which vaporizes the water stems from the energy dissipated at the shock front and is that energy which the shock wave leaves behind in the form of thermal energy after the medium has reexpanded to the initial pressure. Consequently, the water has a higher temperature in this state than it had before the passage of the shock. This temperature increment decreases with increasing distance from the center. Near the center it is high enough not only to vaporize but actually to decompose the water. At greater distances this temperature increment eventually drops to a value which corresponds to the boiling point of water. This condition determines the bubble radius. Since the boiling point is a function of pressure as well as temperature, the mass of water which is evaporated depends on the prevailing pressure, which changes during the expansion of the bubble. Thus the interface is not formed by the same layer of water but is transferred from one set of particles to another. At the moment of the bubble maximum the greatest mass of water is in vapor form. The radius of this maximum bubble is the parameter of primary interest. All the other bubble parameters, such as the first period and the bubble energy, as well as the numerical values of the energy partition, are readily deduced once this magnitude is found.

3.2 DETERMINATION OF MAXIMUM RADIUS

The energy which has been imparted to the water by the explosion can be subdivided into three portions:

1. Shock-wave energy, Q_{SW}.
2. Dissipated energy, Q_{diss}.
3. Bubble energy, Q_B.

The bubble energy is most conveniently found from the difference of total energy and the first two energy terms noted above:

$$Q_B = Q - Q_{SW} - Q_{diss}. \tag{3.1}$$

The shock-wave energy fraction is, according to Eqs. 2.38 and 2.2,

$$\frac{Q_{SW}}{Q} = \frac{\gamma_S}{\eta_1}. \tag{3.2}$$

This magnitude is a function of distance and has been calculated in the previous chapter. Numerical results can be obtained from Table 3.1.

According to Eq. 2.37, the dissipated energy for a shock which has traveled from the distance r_1^* to r_1^θ is

$$Q_{diss} = 4\pi\rho_\theta \int_{r_1^*}^{r_1^\theta} h r_1^2 \, dr_1, \tag{3.3}$$

where h is the dissipated enthalpy increment, Eq. 1.14, and r_1 is the distance of the shock front from the center of the explosion. With the use of Eqs. 1.12, 2.2, and 2.34, we obtain for the dissipated energy fraction

$$\frac{Q_{diss}}{Q} = -\int_{\rho_i}^{\rho_1^*} \frac{2h}{p_1\eta_1\left(\frac{\rho_1 - \rho_\theta}{\rho_\theta}\right)^2}\left[\gamma_{RH}\left(\frac{\rho_1 - \rho_\theta}{\rho_\theta}\right) + 1 + \beta\right] d\rho_1. \tag{3.4}$$

The lower limits of the integrals in Eqs. 3.3 and 3.4 refer to the point at which the shock-wave energy, Eq. 3.1, is calculated. The upper limits of these integrals must be chosen in such a way that the integral covers only those particles which are in the liquid state at the moment of the bubble maximum, since any particle which vaporizes belongs to the interior of the bubble and its energy is counted as bubble energy. Therefore r_1^* designates the layer of particles which forms the interface of the bubble at its maximum expansion, and the sphere having this radius contains the mass of water evaporated. When the shock front has traveled to the distance r_1^*, it encompasses a sphere of average density ρ_θ, the normal density of the water before the explosion. Later, this sphere, consisting of the same particles, has expanded from the radius r_1^* to the maximum bubble radius A_M. Of course, the mass of these two spheres is the same, and therefore

$$\begin{aligned} m &= \int_0^{A_M} dm = 4\pi \int_0^{A_M} \rho r^2 \, dr \\ &= 4\pi \int_0^{r_1^*} \rho_\theta r_1^2 \, dr_1 = \frac{4}{3}\pi\rho_\theta (r_1^*)^3. \end{aligned} \tag{3.5}$$

The volume of the bubble at its maximum is then

$$\begin{aligned} \frac{4}{3}\pi A_M^3 &= \int_0^{A_M} v \, dm \\ &= 4\pi \int_0^{r_1^*} \rho_\theta v(r_1) r_1^2 \, dr_1, \end{aligned} \tag{3.6}$$

where v is the specific volume of the steam inside the bubble at the moment of the maximum expansion. We assume that at this moment the pressure P_M is constant throughout the bubble. Since the bubble interface consists of saturated liquid, this pressure is the saturation pressure P_S of water in the thermodynamic state prevailing at the interface. The pressure P_S and the specific volume v_S of the saturated liquid are functions of the entropy S only and can be readily obtained from the steam tables, such as in reference 17. Thus

$$\begin{aligned} P_M &= P_S(S_{A_M}) \\ v(A_M) &= v_S(S_{A_M}). \end{aligned} \tag{3.7}$$

Also listed in the steam tables is the specific volume of steam at constant pressure as a function of entropy. Therefore we have

$$v(r) = v[S(r),P_{\Delta_1}] = v[S(r),S(A_M)]. \tag{3.8}$$

Since the entropy is constant along the path of a particle, once the shock has passed over it, we have

$$S(A_M) = S(r_1^*)$$

$$S(r) = S(r_1) \tag{3.9}$$

and

$$v(r) = v[S(r_1),S(r_1^*)].$$

This shows that v(r) can be determined with the use of the steam tables and Table 3.1. (The steam tables give the entropy increment above 0°C, whereas Table 3.1 gives that above 8°C. Therefore S(8°C) – S(0°C) must be added to the latter values to bring them on an equal basis.)

The exact evaluation of the integral in Eq. 3.6 is difficult because v increases to infinity when r_1 approaches zero. A rather crude approximation was employed, using Simpson's rule for the evaluation of this integral. The result is shown in Fig. 3.2 (the curve marked Eq. 3.6), where the dimensionless magnitude A_M/r_1^* is plotted vs ρ_1/ρ_0.

To obtain a solution of our problem, we need another independent expression for the magnitude A_M/r_1^*. According to basic bubble theory (Eq. 8.5 of reference 14), the maximum bubble radius and the bubble energy are related by

$$A_M^3 = \frac{3}{4\pi}\alpha_M \frac{Q_B}{P_0}, \tag{3.10}$$

where P_0 is the absolute hydrostatic pressure at firing depth and α_M is a factor which accounts for the internal energy within the bubble. (In the bubble theory, absolute energies are usually used, whereas the energies Q, Q_{SW}, and Q_B are excess energies. These must also be accounted for by α_M.)

Introduction of Eq. 2.2 into Eq. 3.10 yields

$$\left(\frac{A_M}{r_1^*}\right)^3 = 16{,}284\alpha_M \frac{\eta_1 p_1}{Z_0}\frac{\rho_1-\rho_0}{\rho_0}\frac{Q_B}{Q}, \tag{3.11}$$

where Z_0 is the total hydrostatic head in feet and p_1 is in kilobars. Figure 3.2 (the curve marked Eq. 3.11) shows the results obtained from this equation together with Eqs. 3.1 to 3.3. The curve holds for Z_0 = 2033 ft and α_M = 0.8. The lower limit of the integral in Eq. 3.4 was set at $\rho_1^0 = 1.01\rho_0$. From Table 3.1, one finds the corresponding shock-wave energy fraction $Q_{SW}/Q = 0.20$.

The two curves for A_M/r_1^* intersect at the point

$$\frac{\rho_1}{\rho_0} = 1.597 \quad \text{and} \quad \frac{A_M}{r_1^*} = 6.87. \tag{3.12}$$

This establishes the solution of our problem and determines immediately the following magnitudes, as illustrated in Figs. 3.1 and 3.2:

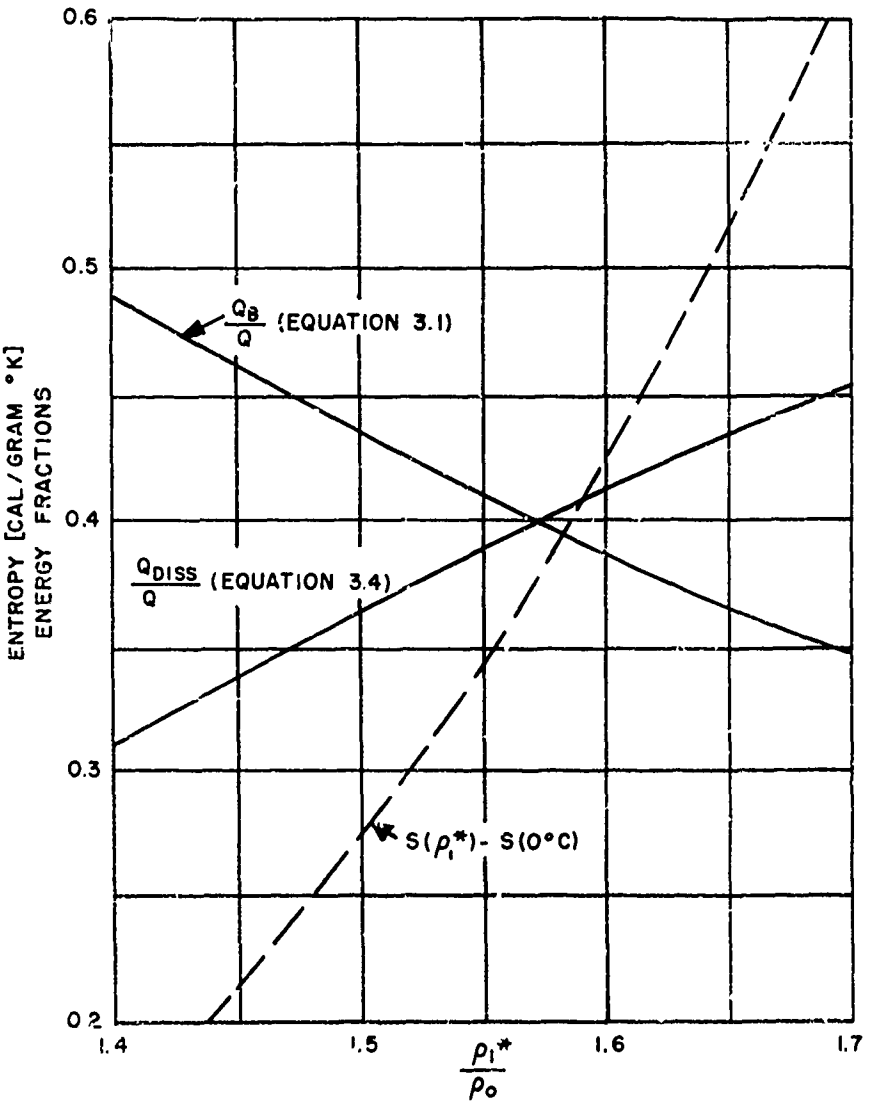

Fig. 3.1 — Dissipated energy, bubble energy, and entropy.

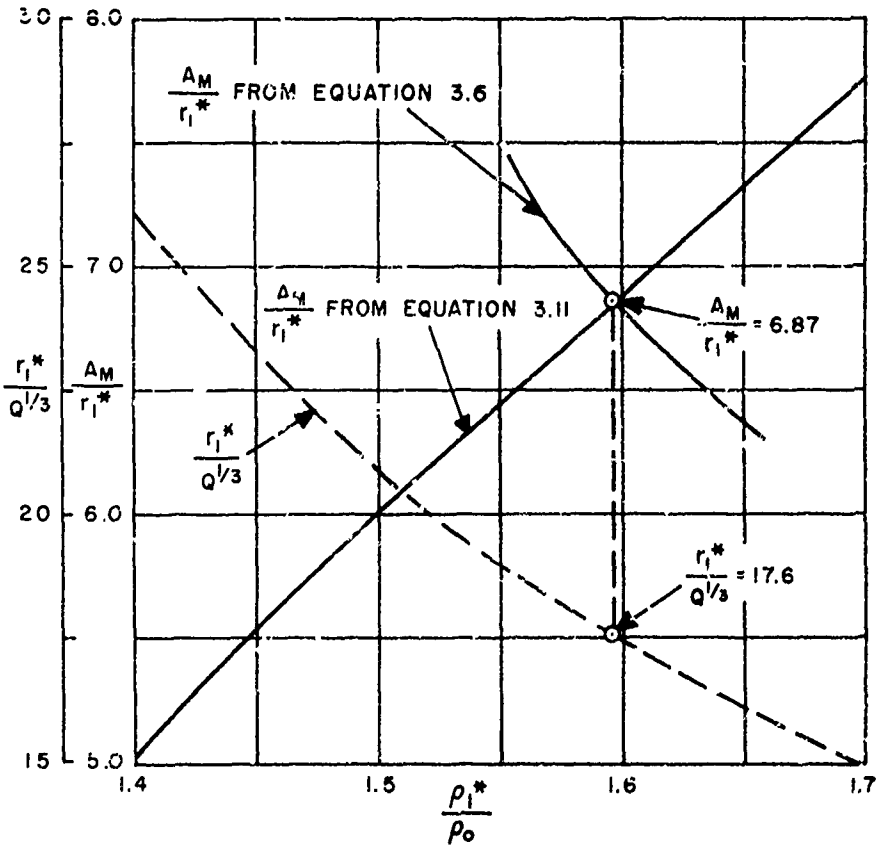

Fig. 3.2 — Determination of the maximum bubble radius.

$$\frac{r_1^*}{Q^{1/3}} = 17.3$$

$$S(A_M) = 0.415 + S\ (0°C) \tag{3.13}$$

$$\frac{Q_B}{Q} = 0.390.$$

3.3 BUBBLE PARAMETERS AND ENERGY PARTITION

From the results in Eqs. 3.12 and 3.13 we find the maximum bubble radius for Q = 30 kt of TNT and Z_0 = 2033 ft:

$$A_M = 373 \text{ ft} \tag{3.14}$$

The corresponding period of the first bubble pulsation T is readily obtained from the experimental evidence that the ratio of the period constant K and the radius constant J are almost the same for all high explosives tested so far.[18] Using the value 0.345, which holds for TNT, we have

$$K = 0.345J$$

$$\frac{T(Z_0)^{5/6}}{W^{1/3}} = 0.345\,\frac{A_M(Z_0)^{1/3}}{W^{1/3}} \tag{3.15}$$

$$T = 0.345\,\frac{A_M}{(Z_0)^{1/2}}.$$

This yields the first bubble period for a 30-kt TNT point explosion at a depth of 2000 ft:

$$T = 2.86 \text{ sec.} \tag{3.15a}$$

Here the question arises whether corrections to the period for surface or bottom effects should be made. (The maximum radius is not changed by these effects.) An approximate formula for such a correction is (see Eq. 16, p. 53 of reference 19):

$$T = T_0\left(1 - 0.2\,\frac{A_M}{D} + 0.2\,\frac{A_M}{B}\right), \tag{3.16}$$

where T_0 = free water period as calculated above
A_M = maximum bubble radius
D = depth of explosion below water surface
B = depth of bottom below center of explosion.

This and similar formulas found in the literature badly overcorrect the bottom effect. They also overcorrect the surface effect for large high-explosive charges once the bubble is several maximum radii below the surface. The latter effect is not so well established as the first one and is not mentioned in the literature, but it is evident from Fig. 8.21 of reference 14. For configurations similar to that considered here (depth about 5⅓ maximum radii), the uncorrected equation seems to give the more accurate result. The period corrected for bottom and surface effects would be 2.79 sec, i.e., about 2 per cent smaller.

In Sec. 3.2 the partition of the three energy terms has been calculated; see also Fig. 3.1. We summarize:

Energy balance:

Bubble energy, 39 per cent of the total energy
Dissipated energy, 41 per cent of the total energy
Shock-wave energy, 20 per cent of the total energy.

The last two terms depend on the distance to which the shock has traveled. They hold for $\rho_1 = 1.01\rho_0$ (which is the value of the lower limit used in the calculation of the integral, Eq. 3.4). This corresponds to the shock-front distance

$$r_1 = 612.4Q^{1/3}$$

or

r_1 = 1903 ft for a 30-kt TNT point explosion.

At larger distances the shock-wave energy decreases as shown in Table 3.1, whereas the dissipated energy increases correspondingly.

3.4 BUBBLE PRESSURE AND TEMPERATURE, MASS OF WATER VAPORIZED

In Sec. 3.2, we have found the entropy on the bubble interface at the moment of the maximum expansion. From the steam tables we can find the corresponding pressure and temperature of the saturated liquid. The first magnitude is equal to the bubble pressure at the moment of the bubble maximum, and the latter refers to the temperature on the bubble interface at the same moment. From the steam tables we find

$$P_M = 52.4 \text{ psia}$$
$$T(A_M) = 284°F. \qquad (3.17)$$

At the maximum bubble radius the bubble pressure has therefore dropped to $1/17.3$ of the hydrostatic pressure and is constant throughout the inside of the bubble. The temperature is constant only within the shell, adjacent to the bubble interface, which contains moist steam. From this point on, the temperature increases rapidly with decreasing distance from the center and, theoretically, reaches infinitely high values at the center.

The density of the medium inside the bubble is, at the interface, that of the saturated liquid (about 0.925 g/cc). The density decreases rapidly with decreasing distance and vanishes at the center.

When the shock front has traveled to the distance r_1^*, it has reached the layer of particles which will be on the bubble interface at the moment of the maximum expansion. The interior of the sphere of radius r_1^* will be, therefore, the interior of the bubble. Hence, the mass of water evaporated is

$$m = \frac{4\pi}{3}\rho_0(r_1^*)^3.$$

We have found in Sec. 3.2 that, for a firing depth of 2000 ft,

$$r_1^* = 17.6Q^{1/3}.$$

This corresponds to a radius

r_1^* = 54.7 ft for Q = 30 kt of TNT.

With a density for sea water of 1.025 g/cc, we find

Maximum mass of water evaporated* = 19.9 metric kt.

It is interesting that the ball of water which is evaporated has just the size of a 30-kt TNT sphere. (The radius of the latter is 55 ft for a loading density of 1.52 g/cc.)

At the moment of the bubble maximum the greatest amount of water is evaporated. When the bubble contracts, the pressure increases and steam condenses at the interface. Thus the interface is transferred to particles which were previously inside the bubble. The condensation will cease when the bubble pressure and temperature have increased to the critical point of water. Beyond this point no condensation is possible, and the mass of the bubble remains constant during any further contraction. This mass will always remain in the vapor state as long as the flow pattern of the bubble pulsation is irrotational, i.e., as long as there is no mixing between the steam and the surrounding cold water. This mass of steam is easily calculated from the entropy-distance relation which can be obtained from Table 3.1. We must determine that shock distance r_1 for which the entropy behind the front is equal to the entropy at the critical point. The latter is $S_{cr} = 1.058 + S\ (0°C)$. The corresponding shock radius is found to be 36 ft, and the mass of water which theoretically always remains in the vapor phase is 5.67 metric kt.

Actually, there will be a strong mixing of different water and steam layers near the bubble minimum for two different reasons. The first is the instability of the interface during the period of time when the bubble is near its minimum. This produces the disintegration of the interface into a spray which is thrown into the interior of the bubble. Obviously, this brings about a thorough mixing of the steam with the surrounding, cooler water. The second phenomenon causing mixing is the distortion of the bubble shape in the gravitational field. When the originally spherical bubble contracts, its lower boundary moves inward faster than the other points of its surface. The cross section of the bubble assumes the shape of a kidney, and finally the lower boundary impinges upon the upper boundary, causing a vast amount of turbulence inside and outside of the bubble. It is for these reasons that the concept of the mass of water which remains in vapor form is misleading and that considerable condensation must be expected at the bubble minima.

3.5 BUBBLE MIGRATION AND LATER BUBBLE PHASES

NAVORD Report 4185 describes a method for the calculation of the bubble oscillation and migration for the second and later cycles. The essential part of these calculations is the determination of the bubble energy for the subsequent cycle. At each minimum the bubble energy is reduced owing to the emission of the bubble pulse and an energy dissipation which is not entirely understood at the present time. Probably it is closely connected with the phenomena described at the end of Sec. 3.4. In NAVORD Report 4185 these energy losses are determined by a semiempirical method which uses experimental data obtained with high explosives. Obviously, these calculations are not valid for steam bubbles. Steam bubbles suffer the same energy losses as gas bubbles do, but in addition there is condensation which damps the oscillation even more. Therefore, the calculations for gas bubbles may be considered as an upper limit for the periods and maximum radii of steam bubbles.

The following results were obtained for gas bubbles:

Second cycle:
- Maximum radius, 368 ft
- Period, 3.40 sec
- Bubble energy, 64 per cent of the bubble energy of the first cycle
- Migration between first and second bubble maxima, 675 ft (There is no appreciable migration up to the moment of the first bubble maximum.)

*The bubble contains a large amount of "wet" steam. Hence, strictly speaking, only a fraction of this mass is in the vapor phase.

Third cycle:
Maximum radius, 330 ft
Period, 4.38 sec
Bubble energy, 18 per cent of the bubble energy of the first cycle
Migration between second and third bubble maxima, 793 ft.

The gas bubble reaches the water surface shortly after the third minimum, about 10.7 sec after the explosion. These results are graphically illustrated in Fig. 3.3. It will be noted that the periods of the later cycles are increased, although the bubble energies are smaller. This is because the bubble has migrated into shallow water where the lower hydrostatic pressure causes the bubble to pulsate more slowly.

Very similar data were obtained experimentally in the vacuum tank.[20,21] In one of these experiments,[21] electric sparks were used to deliver the energy of explosion. The bubbles produced in this way are steam bubbles which should behave very much like the bubbles from atomic underwater explosions. Unfortunately, condensation phenomena are not correctly scaled in such tests. To scale gravity, the pressure above the water surface must be reduced so far that the vapor pressure of water is almost reached. However, for similarity of condensation phenomena, the ratio

$$\frac{\text{Total pressure at firing depth}}{\text{Vapor pressure}}$$

must be the same in full scale as in the model test. Since it is not possible to reduce the vapor pressure of water by the same amount as the total hydrostatic pressure in the tank, condensation cannot be scaled. The conditions in the vacuum tank resemble explosions in almost boiling water, and little condensation is expected under such circumstances. In fact, the test results obtained with sparks and with high-explosive charges are similar and are in good qualitative agreement with the calculated data above.

If in a model experiment which employs electric sparks the air pressure above the water surface is not reduced, gravitational phenomena are not scaled and we have the case of a nonmigrating bubble. The scaling of condensation processes, however, is much improved but still not perfect. Such tests showed strong condensation effects in the second and third cycles. The later periods were substantially less than those of corresponding high explosives, which indicates strongly reduced bubble energies. (The bubble energies of nonmigrating bubbles are proportional to the cubes of the periods.) The pulsations virtually ceased after the third cycle, and, apparently, most of the vapor was condensed.

The following figures give a summary of the results of these tests as well as data referring to TNT explosions:

	Periods relative to the period of the first cycle		
	Cycle 1	Cycle 2	Cycle 3
(a) Nonmigrating TNT bubble	1	0.72	0.59
(b) Nonmigrating steam bubble	1	0.45	0.21
(c) Migrating TNT bubble (Wigwam conditions)	1	1.18	1.52
(d) Crude estimate for migrating steam bubble: (d) = (c) × [(b)/(a)]	1	0.74	0.54

Sources: (a) reference 22, (b) preliminary evaluation of Hudson's tests described in reference 21, (c) calculations based on NAVORD Report 4185 as described in this section.

The first period observed in Operation Wigwam was 2.87 sec, the second, 2.6 sec, and the third, 1.9 sec (reference 15). The ratios of these latter periods to the first period are 0.91 and 0.66, respectively. These values are higher than the above-mentioned crude estimates for the migrating steam bubble but considerably lower than those for the migrating gas bubble. This indicates that substantial condensation must have occurred in Wigwam, although not quite so

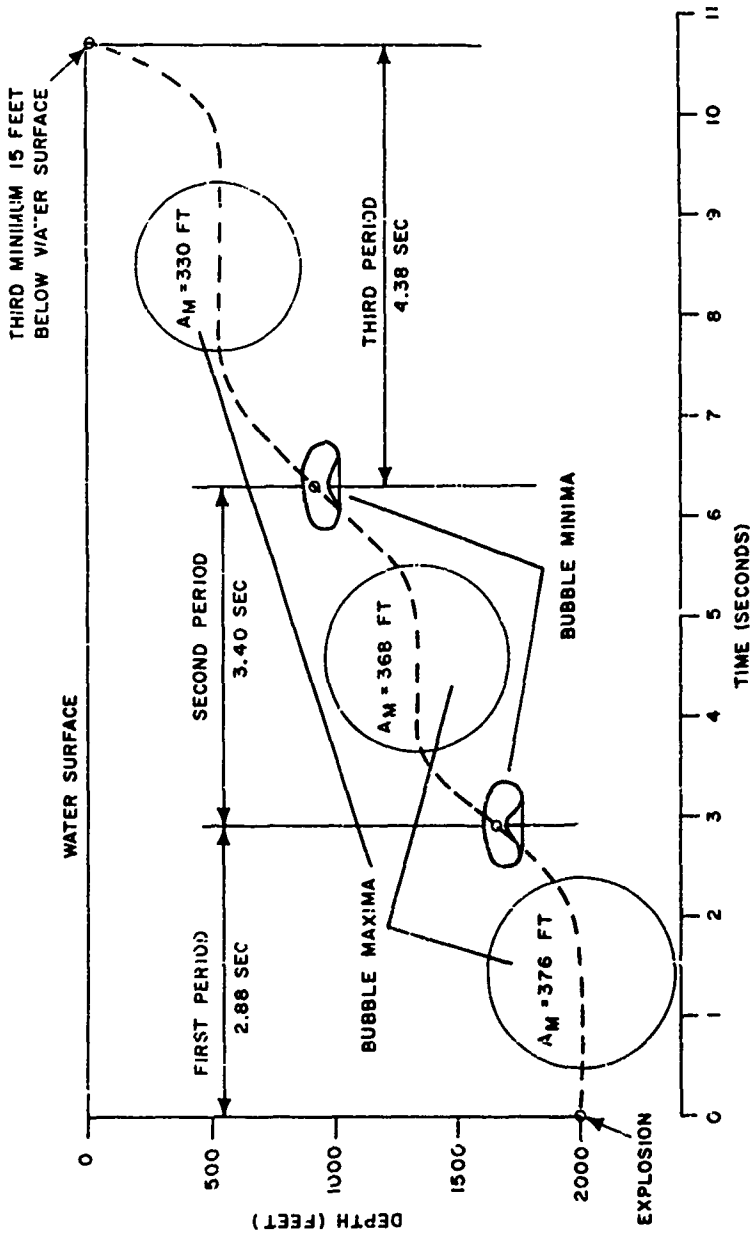

Fig. 3.3—Migration of the gas bubble from 30 kt of TNT.

such as in the case of Hudson's nonmigrating bubble. Actually, however, this model test as well as approximation (d) are much too crude to allow any quantitative conclusions.

Using the concept of the average bubble rise mentioned below, it can be estimated that the third bubble minimum occurred at a depth of about 700 ft. If the bubble would continue to oscillate (which it does if there is still uncondensed vapor), it would have to run through several more cycles before it would reach the water surface. At each minimum more vapor would be condensed, and it seems unlikely that any substantial amount of vapor would be left when the bubble reached the water surface.

This may seem to be in contradiction to the observed surface phenomena which began about 10 sec after the explosion and which showed quite a resemblance to the "breakthrough" of a gas bubble.[23] These phenomena, however, are not necessarily caused by the venting of a steam bubble. At the moments of the first and second bubble maxima, the mass of water near the bubble acquires an upward momentum which produces a flow directed upward. This momentum will be conserved, and the flow will continue even when all the steam is condensed. The violent upwelling of this moving mass of water probably produced the plumes and the surface phenomena of Wigwam.

Figure 3.3 shows that all bubble maxima and minima lie approximately on a straight line. This means that the bubble rises with the same average velocity in each cycle. Condensation would reduce the periods of the oscillation, but the bubble maxima and minima would be approximately on the same line, and the bubble or the water surrounding it would reach the water surface about the same time as the gas bubble. Hence the fact that the plume formation began at the time predicted for a TNT explosion does not necessarily indicate a "TNT-like" bubble behavior.

If all the vapor were condensed, the water would move upward at a constant rate, namely, the above-mentioned average velocity, which is found to be 216 ft/sec. Disregarding air drag, the water would rise 725 ft above the water surface, which is much less than the observed 1400-ft maximum plume height.[23] The latter corresponds to a velocity of 300 ft/sec, which is 40 per cent higher than the average rate of rise. This again is not a proof that the plumes are driven up by expanding gases or vapor, because some portions of the moving mass of water can have higher velocities than its rate of rise. For instance, a suitable hydrodynamic model of such a moving mass of water is a vortex ring. (Vortex rings have been actually observed with high explosives fired at great depth.) The total kinetic energy of such a vortex ring is larger than its translational kinetic energy. When reaching the water surface, some of its particles will rise much higher than the average calculated from the translational energy.

These considerations show that the phenomena observed in Wigwam are not in contradiction to the possibility that all the steam is condensed in the later bubble oscillations. Complete condensation, however, must not be expected. For instance, all the gases dissolved in the evaporated water will remain, and combined with these will be a certain amount of water vapor. This is clearly visible in the model tests, but an estimate of its magnitude is difficult and has not been attempted. For practical purposes this amount is probably negligibly small, and it seems safe to state that essentially all the vapor was condensed in Wigwam before the bubble reached the surface.

3.6 SUMMARY

The bubble period of an atomic explosion of 30-kt yield at a depth of 2000 ft under water was calculated to be 2.88 sec. A 24.35-kt TNT charge detonated at the same depth would have the same period.

The measured bubble period in Wigwam is 2.87 sec. In view of the approximations made in the calculations, such good agreement was not expected.

At the bubble maximum, 19.9 kt of water are in the vapor form. The liquid producing this would make a sphere of the same size as a 30-kt TNT sphere.

Data for a migrating bubble of a 24.35-kt TNT explosion are presented in Sec. 3.5 and are illustrated in Fig. 3.3. The gas bubble reaches the water surface about 11 sec after the detona-

tion. Comparison with model tests using electric sparks as energy sources indicates that the steam bubbles produced by atomic explosions must behave somewhat differently. There will be condensation of vapor at the bubble minima. Very little vapor is expected to reach the water surface. The plumes observed in Wigwam about 10 sec after the explosion are probably produced by the violent upwelling of water which originally surrounded the bubble. This water keeps on moving upward even when all steam is condensed.

Table 3.1—SHOCK-FRONT AND SHOCK-WAVE PARAMETERS

Shock-front parameters							Shock-wave parameters										
							Reduced magnitudes						Yield (Q) = 10 kt of TNT				
Density ratio	Pressure	Temperature	Isentropic exponent	Hankin Hugoniot factor	Entropy increment (0°C initial temp.)	Reduced enthalpy increment	Total energy	$\frac{d \ln \eta_1}{d \ln\left(\frac{\rho_1 - \rho_2}{\rho_2}\right)}$	Distance	Arrival time	Time constant	Shock-wave energy ratio	Peak pressure	Distance	Arrival time	Time constant	Shock-wave energy
ρ_1/ρ_0	p_1, lb	T_1, °K	γ_1	$\gamma_{Hk} \frac{\rho_1 - \rho_0}{\rho_1}$	ΔS, cal/g-°K	$\frac{\rho_0 h}{p_0\left(\frac{\rho_1 - \rho_0}{\rho_0}\right)^2}$	η_1	β	$r_1/Q^{1/3}$, ft/(kt)$^{1/3}$	$t/Q^{1/3}$, msec/(kt)$^{1/3}$	$\theta/Q^{1/3}$, msec/(kt)$^{1/3}$	$\frac{1}{4\pi} \frac{E_s}{\eta_1}$	p_1, 10^4 psi	r_1, ft	t, msec	θ, msec	E_{sw}, 10^4 in.-lb/in.^{2}
4.00	∞	∞	1.67	∞			0.66	−1.50	0.000	0.0000	0.0000		∞	0.000	0.000	0.0000	
3.60	48,041		1.33	16.035	9.85		0.80	−1.32	1.912	0.0052	0.0007		705,300	5.940	0.016	0.0022	
3.20	10,278	80,000	1.29	5.878	5.35		1.00	−1.16	3.149	0.0106	0.0028		14,900	9.784	0.033	0.0087	
2.80	3,815	25,000	1.18	4.421	3.67		1.27	−1.00	4.325	0.0228	0.0069		5,532	13.44	0.071	0.0214	
2.40	1,321	8,100	1.50	4.039	2.43		1.60	−0.85	6.205	0.0536	0.0162		1,915	19.23	0.167	0.0505	
2.20	727.1	4,250	1.77	3.749	1.59		1.80	−0.75	7.663	0.0859	0.0314		1,054	23.81	0.267	0.0975	
2.00	377.4	2,120	4.02	3.436	1.36	0.090	2.05	−0.66	9.701	0.1507	0.0564		547.2	30.14	0.468	0.1752	
1.90	246.9	1,380	4.13	3.235	1.10	0.118	2.20	−0.61	11.32	0.2044	0.0773		356.7	35.18	0.635	0.2401	
1.80	182.8	1,062	4.39	3.065	0.80	0 123	2.36	−0.56	12.80	0.2703	0.1074		265.1	39.44	0.858	0.3337	
1.75	145.0	878	4.52	2.930	0.70	0.148	2.44	−0.53	13.52	0.3250	0.1282		207.4	43.27	1.01	0.3965	
1.70	120.8	770	4.68	2.825	0.55	0 161	2.52	−0.50	14.93	0.3843	0.1551		174.0	46.38	1.19	0.4819	
1.60	81.4	600	5.04	2.590	0.396	0 196	2.71	−0.44	17.47	0.5503	0.2246	0.0323	118.1	54.29	1.71	0.6960	8,465
1.50	53.2	495	5.50	2.337	0.245	0.246	2.92	−0.37	20.88	0.8017	0.3340	0.0310	77.14	64.89	2.49	1.038	5,980
1.40	32.0	415	6.24	2.079	1.30×10^{-1}	0.319	3.16	−0.28	25.80	1.229	0.5277	0.0305	46.40	80.76	3.62	1.640	3,613
1.30	18.0	362	7.40	1.866	5.80×10^{-2}	0.418	3.40	−0.18	33.77	2.010	0.8672	0.0293	26.18	104.9	6.25	2.757	2,054
1.20	8.796	324	9.44	1.672	1.80×10^{-2}	0.536	3.50	−0.04	48.58	3.832	1.659	0.0282	12.75	150.9	11.91	5.154	953.7
1.175	6.500	315	10.30	1.621	9.40×10^{-3}	0.548	3.50	0.00	55.94	4.899	2.116	0.0281	9.256	173.8	14.6	6.576	719.4
1.150	5.127	300	11.13	1.534	5.50×10^{-3}	0.557	3.50	+0.05	64.02	5.962	2.565	0.0280	7.435	198.9	18.2	7.785	597.5
1.125	3.912	305	12.38	1.439	2.95×10^{-3}	0.560	3.48	0.10	74.5	7.060	3.044	0.0145	5.672	231.7	23.8	9.460	351.8
1.100	2.886	300.7	14.43	1.355	1.30×10^{-3}	0.563	3.37	0.16	89.86	10.07	3.835	0 0258	4.184	279.2	31.3	11.89	235.4
1.075	2.000	296.0	17.44	1.242	5.40×10^{-4}	0.562	3.17	0.23	113.9	14.16	4.730	0.0216	2.911	354.1	44.0	14.76	132.7
1.050	1.340	295.8	23.84	1.135	1.43×10^{-4}	0.563	2.80	0.32	159.2	22.59	6.026	0.0200	1.810	494.7	70.2	18.72	63.12
1.025	0.864	296.2	43.80	1.063	1.75×10^{-5}	0.563	2.16	0.437	231.9	45.38	8.163	0.0174	0.8475	875.5	141	25.36	17.47
1.020	0.682	293.9	53.57	1.051	7.84×10^{-6}	0.563	1.946	0.465	340.2	57.43	8.733	0.0168	0.6006	1,051	178	27.14	11.60
1.015	0.542	293.7	70.20	1.038	3.68×10^{-6}	0.563	1.70	0.502	432.5	70.27	9.570	0.0151	0.4968	1,344	237	29.74	6.89
1.010	0.325	293.5	103.43	1.025	1.08×10^{-6}	0.563	1.364	0.546	612.4	112.6	10.13	0.0136	0.3267	1,902	350	33.35	3.32
1.005	0.211	293.3	203.40	1.011	1.33×10^{-7}	0.563	0.899	0.635	1,122.2	217.1	12.74	0.0150	0.1814	3,487	675	39.60	0.95

REFERENCES

1. H. G. Snay and R. H. Matthias, A Theory of the Propagation of Shock Waves and Their Formation by Explosions, NAVORD Report 2195, 1951.
2. E. A. Christian and H. G. Snay, Analysis of Experimental Data on Detonation Velocities, NAVORD Report 1508, 1951.
3. R. V. Meghreblian, Thermodynamic Functions of Polyelectronic Atoms at Very High Temperatures, Technical Report No. 7, California Institute of Technology, 1952.
4. R. H. Fowler, "Statistical Mechanics," Cambridge University Press, 1955.
5. H. Jones, The Properties of Gases at High Pressures Which Can Be Deduced from Explosion Experiments, Third Symposium on Combustion and Flame and Explosion Phenomena, The Williams & Wilkins Company, 1949.
6. John G. Kirkwood and Elliott W. Montroll, The Pressure Wave Produced by an Underwater Explosion II, OSRD Report No. 670, 1942.
7. John G. Kirkwood and John M. Richardson, The Pressure Wave Produced by an Underwater Explosion III, OSRD Report No. 813, 1942.
8. H. G. Snay and J. H. Rosenbaum, Shock-wave Parameters in Fresh Water for Pressures Up to 95 Kilobars, NAVORD Report 2383, 1952.
9. John G. Kirkwood and Hans A. Bethe, The Pressure Wave Produced by an Underwater Explosion I, OSRD Report No. 588, 1942.
10. T. A. Litovitz and E. H. Carnevale, Pressure Dependence of Ultrasonic Velocity in Sea Water, J. Acoust. Soc. Amer., 27: 794 (1955).
11. J. M. Walsh and M. H. Rice, Equation of State of Water, Los Alamos Scientific Laboratory, private communication to Explosives Research Department, NOL, 1955.
12. Joseph Weber, private communications to Explosives Research Department, NOL, dated 8 February 1954, 12 April 1954, 11 May 1954, 2 June 1954, and 13 September 1954.
13. G. I. Taylor, The Formation of a Blast Wave by a Very Intense Explosion, Proc. Roy. Soc., A201: 159 (1950).
14. Robert H. Cole, "Underwater Explosions," Princeton University Press, 1948.
15. C. J. Aronson et al., Underwater Free-field Pressures to Just Beyond Target Locations, Operation Wigwam Report, WT-1005 (in preparation).
16. F. B. Porzel, Close-in Time of Arrival of Underwater Shock Wave, Operation Wigwam Report, WT-1034 (in preparation).
17. Joseph H. Keenan and Frederick G. Keyes, "Thermodynamic Properties of Steam," John Wiley & Sons, 1936.
18. Bureau of Ships, Fourth Conference on Research on Ship Protection Against Underwater Explosions, December 1952, NavShips-250-423-14, p. 246.
19. E. H. Kennard, Underwater Explosions: A Summary of Results, DTMB Report C-334, February 1951.
20. John F. Goertner, Vacuum Tank Studies of Underwater Explosion Bubbles Scaled to the Nuclear Range, NAVORD Report 3714, 1954.

21. George E. Hudson, Summary Report of the Bubble Oscillation Project, New York University, Contract NOrd 14663, 1955.
22. A. B. Aron:, Bubble Pulse Phenomena IV: Pressure-Time Measurements in Free Water, NAVORD Report 408, 1947.
23. G. A. Young et al., Photographic Measurements of Surface Phenomena, Operation Wigwam Report, WT-1009 (in preparation).

APPENDIX A

GLOSSARY OF SYMBOLS

a_1, a_2	Abbreviations defined by Eqs. 1.38 and 1.39
A_i	*i*th coefficient in the expansion of the reduced pressure about the center
A_M	Maximum bubble radius
B_i	*i*th coefficient in the expansion of the reduced density about the center
B	Depth of bottom below the center of the explosion
C_i	*i*th coefficient in the expansion of the reduced velocity about the center
C	Integration constant in Eq. 2.43a
c	Velocity of sound; parameter in TFD theory; constant in Eq. 2.32
c_∞	Velocity of sound in the undisturbed medium
$c^0_{v_i}$	Ideal-gas heat capacity at constant volume for the *i*th constituent
$c^0_{p_i}$	Ideal-gas heat capacity at constant pressure for the *i*th constituent
$\bar{c}_v, \overline{c_p}$	Average heat capacities defined by Eq. 1.16
e	2.71828...; electronic charge
D	Depth of explosion below water surface
E	Internal energy per unit mass
E_1	Internal energy per unit mass directly behind the shock front
E_∞	Internal energy per unit mass in the undisturbed medium
E_{SW}	Shock-wave energy flux
f	Shape factor
g_i	Statistical weight of the *i*th excited state of an atom, ion, or molecule
G_1	Decay factor of the shock-wave peak density, Eq. 2.11
h	Dissipated enthalpy increment; Planck's constant
H_1	Decay factor of the shock-wave peak pressure, Eq. 2.10
J	Reduced internal energy
J_1	Reduced internal energy directly behind the shock front
J^0	Reduced internal energy of an ideal gas
k_i	Covolume factor for the *i*th constituent
k_e	Covolume factor for a component when in its ground state
k	Total covolume factor
k'	Boltzmann's constant
K_j	Equilibrium constant for the *j*th chemical reaction
$K^0_{p_j}$	Ideal-gas equilibrium constant for the *j*th chemical reaction
ln	Natural logarithm
log	Logarithm to the base 10
L_1	Decay factor for the shock-wave peak particle velocity, Eq. 2.12
m	$= 3(\gamma^0 - 1)$; particle mass; total mass of the sphere encompassed by the shock front

M_0	Molecular weight of water
M	Number of hydrogen nuclei per cell in the TFD theory
n_i	Number of moles of the i*th* constituent in M_0 grams of the mixture
n_ℓ	Total number of moles in M_0 grams
N_{Av}	Avogadro's number
p	Excess pressure
p_1	Shock-wave peak pressure
p_T	Thermal pressure
P_0	Absolute pressure in the undisturbed medium
P_{ij}	Coefficients in Eqs. 2.46 and 2.47
P_M	Pressure in the steam bubble at the moment of the maximum radius
P_S	Pressure of the saturated liquid
Q	Energy yield in kilotons of TNT; partition function
Q_{diss}	Dissipated energy
Q_B	Bubble energy
r_{ij}	Coefficients in Eq. 1.24
r	Radius
r_1	Radius of shock front
r_1^*	Radius of the layer of particles which forms the bubble interface at its maximum expansion
r_0	Reference radius
R	Gas constant
$\mathcal{R}$	Cell radius in TFD theory
S	Entropy per unit mass
S_1	Entropy per unit mass directly behind the shock front
S_0	Entropy per unit mass in the undisturbed medium
S_{AM}	Entropy per unit mass at the bubble maximum
S_{cr}	Entropy per unit mass at the critical point
t	Time
T	Temperature; first bubble period
T_0	Free-water bubble period
u	Particle velocity
u_1	Particle velocity directly behind the shock front
u_0	Particle velocity in the undisturbed medium
U	Propagation velocity of the shock front
v	Specific volume
v_S	Specific volume of the saturated liquid
V_j	Effective atomic or ionic volume of a component in its ground state
V_i	Effective atomic or ionic volume of a component when in its i*th* excited state
w_i	Coefficients in Eq. 2.49
W	Energy yield in pounds of TNT
x	Imperfection factor in the HKW equation of state, Eq. 1.17; reduced radius in TFD and Snay-Matthias theories
π	$= (\rho_1 - \rho_0)/\rho_0$
y_1	Number of moles of hydrogen atoms in M_0 grams of the mixture
y_2	Number of moles of oxygen atoms in M_0 grams of the mixture
y_3	Number of moles of free electrons in M_0 grams of the mixture
Z	Charge of the oxygen nucleus
Z_i	Valency of the i*th* component
Z_j	Valency of the j*th* reaction
Z_0	Total hydrostatic head in feet
α	Time factor; parameter in HKW equation of state
α_M	Factor which accounts for the internal energy within the bubble
β	Logarithmic decay factor for the reduced total energy; parameter in HKW equation of state

β_0	Exchange correction
β_S	Logarithmic decay factor for the reduced shock-wave energy
γ	Isentropic exponent, Eq. 1.9
γ_1	Isentropic exponent directly behind the shock front
γ^0	Isentropic exponent for an ideal gas
γ_{RP}	Logarithmic derivative of the peak pressure with respect to the peak density
ϵ_i	Excitation energy of the *i*th excited state of an atom, ion, or molecule
η_1	Reduced total energy, Eq. 2.3
η_S	Reduced shock-wave energy
ξ	Reduced radius
ν_i	Stoichiometric coefficient of the *i*th component in a chemical reaction
π	3.141585...
ρ	Density
ρ_1	Density directly behind the shock front
ρ_0	Density of the undisturbed medium
μ	Thomas-Fermi unit
ζ	Coefficient in Eq. 1.34
Φ	Electrostatic correction, Eq. 1.23
φ	Reduced particle velocity
φ_1^n	*n*th derivative of φ with respect to ξ, evaluated at $\xi = 1$
χ	Reduced density
ψ	Reduced pressure
Ψ	TFD potential
θ	Time constant

DISTRIBUTION

Military Distribution Category 5-23

ARMY ACTIVITIES

Asst. Dep. Chief of Staff for Military Operations, Washington 25, D. C. ATTN: Asst. Executive (R&SW)	1
Chief of Research andDevelopment, D/A, Washington 25, D. C. ATTN: Atomic Division	2
Chief of Ordnance, D/A, Washington 25, D. C. ATTN: ORDTX-AR	3
Chief Signal Officer, D/A, P&O Division, Washington 25, D. C. ATTN: SIGOP	4-6
The Surgeon General, D/A, Washington 25, D. C. ATTN: Chief, R&D Division	7
Chief Chemical Officer, D/A, Washington 25, D. C.	8-9
The Quartermaster General, D/A, Washington 25, D. C. ATTN: Research and Development Div.	10
Chief of Engineers, D/A, Washington 25, D. C. ATTN: ENGNB	11-15
Chief of Transportation, Military Planning and Intelligence Div., Washington 25, D. C.	16
Commanding General, Continental Army Command, Ft. Monroe, Va.	17-19
President, Board #1, Headquarters, Continental Army Command, Ft. Sill, Okla.	20
President, Board #2, Headquarters, Continental Army Command, Ft. Knox, Ky.	21
President, Board #4, Headquarters, Continental Army Command, Ft. Bliss, Tex.	22
Commanding General, U. S. Army Caribbean, Ft. Amador, C. Z. ATTN: Cml. Off.	23
Commander-in-Chief, Far East Command, APO 500, San Francisco, Calif. ATTN: ACofS, J-3	24-25
Commanding General, U. S. Army Europe, APO 403, New York, N. Y. ATTN: OPOT Div., Combat Dev. Br.	26-27
Commanding General, U. S. Army Pacific, APO 958, San Francisco, Calif. ATTN: Cml. Off.	28-29
Commandant, Command and General Staff College, Ft. Leavenworth, Kans. ATTN: ALLLS(AS)	30-31
Commandant, The Artillery and Guided Missile School, Ft. Sill, Okla.	32
Secretary, The Antiaircraft Artillery and Guided Missile School, Ft. Bliss, Tex. ATTN: Maj Gregg D. Breitegan, Dept. of Tactics and Combined Arms	33
Commanding General, Army Medical Service School, Brooke Army Medical Center, Ft. Sam Houston, Tex.	34
Director, Special Weapons Development Office, Headquarters, CONARC, Ft. Bliss, Tex. ATTN: Capt T. E. Skinner	35
Commandant, Walter Reed Army Institute of Research, Walter Reed Army Medical Center, Washington 25, D. C.	36
Superintendent, U. S. Military Academy, West Point, N. Y. ATTN: Prof. of Ordnance	37
Commandant, Chemical Corps School, Chemical Corps Training Command, Ft. McClellan, Ala.	38
Commanding General, Research and Engineering Command, Army Chemical Center, Md. ATTN: Deputy for RW and Non-Toxic Material	39
Commanding General, The Engineer Center, Ft. Belvoir, Va. ATTN: Asst. Commandant, Engineer School	40-42
Commanding Officer, Engineer Research and Development Laboratory, Ft. Belvoir, Va. ATTN: Chief, Technical Intelligence Branch	43

Commanding Officer, Picatinny Arsenal, Dover, N. J. ATTN: ORDBB-TK	44	44
Commanding Officer, Army Medical Research Laboratory, Ft. Knox, Ky.	45	45
Commanding Officer, Chemical Corps Chemical and Radiological Laboratory, Army Chemical Center, Md. ATTN: Tech. Library	46--47	46--47
Commanding Officer, Transportation R&D Station, Ft. Eustis, Va.	48	48
Director, Technical Documents Center, Evans Signal Laboratory, Belmar, N. J.	49	49
Director, Waterways Experiment Station, PO Box 631, Vicksburg, Miss. ATTN: Library	50	50
Director, Armed Forces Institute of Pathology, Walter Reed Army Medical Center, 6825 16th Street, N.W., Washington 25, D. C.	51	51
Director, Operations Research Office, Johns Hopkins University, 7100 Connecticut Ave., Chevy Chase, Md., Washington 15, D. C.	52	52
Commanding General, Quartermaster Research and Development Command, Quartermaster Research and Development Center, Natick, Mass. ATTN: CSR Liaison Officer	53--54	53--54
NAVY ACTIVITIES		
Chief of Naval Operations, D/N, Washington 25, D. C. ATTN: OP-36	55--56	55--56
Chief of Naval Operations, D/N, Washington 25, D. C. ATTN: OP-03EG	57	57
Director of Naval Intelligence, D/N, Washington 25, D. C. ATTN: OP-922V	58	58
Chief, Bureau of Medicine and Surgery, D/N, Washington 25, D. C. ATTN: Special Weapons Defense Div.	59	59
Chief, Bureau of Ordnance, D/N, Washington 25, D. C.	60	60
Chief, Bureau of Ships, D/N, Washington 25, D. C. ATTN: Code 348	61	61
Chief, Bureau of Yards and Docks, D/N, Washington 25, D. C. ATTN: D-440	62	62
Chief, Bureau of Supplies and Accounts, D/N, Washington 25, D. C.	63	63
Chief, Bureau of Aeronautics, D/N, Washington 25, D. C.	64--65	64--65
Chief of Naval Research, Department of the Navy, Washington 25, D. C. ATTN: Code 811	66	66
Commander-in-Chief, U. S. Pacific Fleet, Fleet Post Office, San Francisco, Calif.	67	67
Commander-in-Chief, U. S. Atlantic Fleet, U. S. Naval Base, Norfolk 11, Va.	68	68
Commandant, U. S. Marine Corps, Washington 25, D. C. ATTN: Code A03H	69--72	69--72
President, U. S. Naval War College, Newport, R. I.	73	73
Superintendent, U. S. Naval Postgraduate School, Monterey, Calif.	74	74
Commanding Officer, U. S. Naval Schools Command, U. S. Naval Station, Treasure Island, San Francisco, Calif.	75	75
Commanding Officer, U. S. Fleet Training Center, Naval Base, Norfolk 11, Va. ATTN: Special Weapons School	76	76
Commanding Officer, U. S. Fleet Training Center, Naval Station, San Diego 36, Calif. ATTN: (SPWP School)	77	77
Commanding Officer, U. S. Naval Damage Control Training Center, Naval Base, Philadelphia 12, Pa. ATTN: ABC Defense Course	78	78
Commanding Officer, U. S. Naval Unit, Chemical Corps School, Army Chemical Training Center, Ft. McClellan, Ala.	79	79
Commander, U. S. Naval Ordnance Laboratory, Silver Spring 19, Md. ATTN: EE	80	80
Commander, U. S. Naval Ordnance Laboratory, Silver Spring 19, Md. ATTN: EH	81	81
Commander, U. S. Naval Ordnance Laboratory, Silver Spring 19, Md. ATTN: R	82	82
Commander, U. S. Naval Ordnance Test Station, Inyokern, China Lake, Calif.	83	83
Officer-in-Charge, U. S. Naval Civil Engineering Res. and Evaluation Lab., U. S. Naval Construction Battalion Center, Port Hueneme, Calif. ATTN: Code 753	84	84
Commanding Officer, U. S. Naval Medical Research Inst., National Naval Medical Center, Bethesda 14, Md.	85	85
Director, Naval Air Experimental Station, Air Material Center, U. S. Naval Base, Philadelphia, Pa.	86	86
Director, U. S. Naval Research Laboratory, Washington 25, D. C. ATTN: Mrs. Katherine H. Cass	87	87
Commanding Officer and Director, U. S. Navy Electronics Laboratory, San Diego 52, Calif. ATTN: Code 4223	88	88
Commanding Officer, U. S. Naval Radiological Defense Laboratory, San Francisco 24, Calif. ATTN: Technical Information Division	89--90	89--90
Commanding Officer and Director, David W. Taylor Model Basin, Washington 7, D. C. ATTN: Library	91	91
Commander, U. S. Naval Air Development Center, Johnsville, Pa.	92	92

Commanding Officer, Picatinny Arsenal, Dover, N. J. ATTN: ORDBB-TK	44	44
Commanding Officer, Army Medical Research Laboratory, Ft. Knox, Ky.	45	45
Commanding Officer, Chemical Corps Chemical and Radiological Laboratory, Army Chemical Center, Md. ATTN: Tech. Library	46--47	46--47
Commanding Officer, Transportation R&D Station, Ft. Eustis, Va.	48	48
Director, Technical Documents Center, Evans Signal Laboratory, Belmar, N. J.	49	49
Director, Waterways Experiment Station, PO Box 631, Vicksburg, Miss. ATTN: Library	50	50
Director, Armed Forces Institute of Pathology, Walter Reed Army Medical Center, 6825 16th Street, N.W., Washington 25, D. C.	51	51
Director, Operations Research Office, Johns Hopkins University, 7100 Connecticut Ave., Chevy Chase, Md., Washington 15, D. C.	52	52
Commanding General, Quartermaster Research and Development Command, Quartermaster Research and Development Center, Natick, Mass. ATTN: CSR Liaison Officer	53--54	53--54
NAVY ACTIVITIES		
Chief of Naval Operations, D/N, Washington 25, D. C. ATTN: OP-36	55--56	55--56
Chief of Naval Operations, D/N, Washington 25, D. C. ATTN: OP-03EG	57	57
Director of Naval Intelligence, D/N, Washington 25, D. C. ATTN: OP-922V	58	58
Chief, Bureau of Medicine and Surgery, D/N, Washington 25, D. C. ATTN: Special Weapons Defense Div.	59	59
Chief, Bureau of Ordnance, D/N, Washington 25, D. C.	60	60
Chief, Bureau of Ships, D/N, Washington 25, D. C. ATTN: Code 348	61	61
Chief, Bureau of Yards and Docks, D/N, Washington 25, D. C. ATTN: D-440	62	62
Chief, Bureau of Supplies and Accounts, D/N, Washington 25, D. C.	63	63
Chief, Bureau of Aeronautics, D/N, Washington 25, D. C.	64--65	64--65
Chief of Naval Research, Department of the Navy, Washington 25, D. C. ATTN: Code 811	66	66
Commander-in-Chief, U. S. Pacific Fleet, Fleet Post Office, San Francisco, Calif.	67	67
Commander-in-Chief, U. S. Atlantic Fleet, U. S. Naval Base, Norfolk 11, Va.	68	68
Commandant, U. S. Marine Corps, Washington 25, D. C. ATTN: Code A03H	69--72	69--72
President, U. S. Naval War College, Newport, R. I.	73	73
Superintendent, U. S. Naval Postgraduate School, Monterey, Calif.	74	74
Commanding Officer, U. S. Naval Schools Command, U. S. Naval Station, Treasure Island, San Francisco, Calif.	75	75
Commanding Officer, U. S. Fleet Training Center, Naval Base, Norfolk 11, Va. ATTN: Special Weapons School	76	76
Commanding Officer, U. S. Fleet Training Center, Naval Station, San Diego 36, Calif. ATTN: (SPWP School)	77	77
Commanding Officer, U. S. Naval Damage Control Training Center, Naval Base, Philadelphia 12, Pa. ATTN: ABC Defense Course	78	78
Commanding Officer, U. S. Naval Unit, Chemical Corps School, Army Chemical Training Center, Ft. McClellan, Ala.	79	79
Commander, U. S. Naval Ordnance Laboratory, Silver Spring 19, Md. ATTN: EE	80	80
Commander, U. S. Naval Ordnance Laboratory, Silver Spring 19, Md. ATTN: EH	81	81
Commander, U. S. Naval Ordnance Laboratory, Silver Spring 19, Md. ATTN: R	82	82
Commander, U. S. Naval Ordnance Test Station, Inyokern, China Lake, Calif.	83	83
Officer-in-Charge, U. S. Naval Civil Engineering Res. and Evaluation Lab., U. S. Naval Construction Battalion Center, Port Hueneme, Calif. ATTN: Code 753	84	84
Commanding Officer, U. S. Naval Medical Research Inst., National Naval Medical Center, Bethesda 14, Md.	85	85
Director, Naval Air Experimental Station, Air Material Center, U. S. Naval Base, Philadelphia, Pa.	86	86
Director, U. S. Naval Research Laboratory, Washington 25, D. C. ATTN: Mrs. Katherine H. Cass	87	87
Commanding Officer and Director, U. S. Navy Electronics Laboratory, San Diego 52, Calif. ATTN: Code 4223	88	88
Commanding Officer, U. S. Naval Radiological Defense Laboratory, San Francisco 24, Calif. ATTN: Technical Information Division	89--90	89--90
Commanding Officer and Director, David W. Taylor Model Basin, Washington 7, D. C. ATTN: Library	91	91
Commander, U. S. Naval Air Development Center, Johnsville, Pa.	92	92

ATOMIC ENERGY COMMISSION ACTIVITIES

U. S. Atomic Energy Commission, Classified Technical Library, 1901 Constitution Ave., Washington 25, D. C. ATTN: Mrs. J. M. O'Leary (for DMA)	163–165
Los Alamos Scientific Laboratory, Report Library, PO Box 1663, Los Alamos, N. Mex. ATTN: Helen Redman	166–167
Sandia Corporation, Classified Document Division, Sandia Base, Albuquerque, N. Mex. ATTN: Martin Lucero	168–172
University of California Radiation Laboratory, PO Box 808, Livermore, Calif. ATTN: Clovis G. Craig	173–175
Weapon Data Section, Technical Information Service Extension, Oak Ridge, Tenn.	176
Technical Information Service Extension, Oak Ridge, Tenn. (surplus)	177–204

ADDITIONAL DISTRIBUTION

Commander, Operational Development Force, United States Atlantic Fleet, United States Naval Base, Norfolk 11, Va.	205

AEC, Oak Ridge, Tenn.

AFBMD Library Charge-Out Card

Document No: K-511 Copy No: 1 O/A Report No:
Title: OPERATION WIGWAM
PREDICTIONS OF UNDERWATER EXPLOSION PHENOMENA Class:

Orig. Ag'y: COMMANDER TASK GROUP 7.3

Author: SWAY BUTLER GLEYZAL Doc. Date: MAY 1955

Borrower's Name	Date Out.	Date In	Borrower's Signature
1st. LT. RALPH DUDLEY WDIE	10/28/59	NOV 9 1959	Ralph A. D.

AFBMD Library Charge-Out Card

Document No: K-511 Copy No: 1 O/A Report No: WT-1004
Title: OPERATION WIGWAM (BOLR-1213)
PREDICTIONS OF UNDERWATER EXPLOSION PHENOMENA Class: U

Orig. Ag'y: COMMANDER TASK GROUP 7.3

Author: SWAY BUTLER GLEYZAL Doc. Date: MAY 1955 Contract No:

Borrower's Name	Date Out.	Date In	Borrower's Signature
1st. LT. RALPH DUDLEY WDIE	10/28/59	NOV 9 1959	Ralph A. Dudley

AFBMD Library Charge-Out Card

Copy No: 2

Contract No.

Borrower's Name	Date Out	Date In	Borrower's Signature
		NOV 9 1959